COMPUTATIONAL APPROACHES TO EFFICIENTLY MAXIMIZE SOLUTION CAPABILITIES AND QUANTIFY UNCERTAINTY FOR INVERSE PROBLEMS IN MECHANICS

by

Bahram Notghi

BS in Mechanical Engineering, Azad University, Iran, 2006

MS in Mechanical Engineering, Azad University, Iran, 2009

Submitted to the Graduate Faculty of

the Swanson School of Engineering in partial fulfillment

of the requirements for the degree of

Doctor of Philosophy

University of Pittsburgh

2014

UNIVERSITY OF PITTSBURGH

SWANSON SCHOOL OF ENGINEERING

This dissertation was presented

by

Bahram Notghi

It was defended on

July 24th, 2014

and approved by

John C. Brigham, PhD, Assistant Professor, Department of Civil and Environmental

Engineering and Bioengineering

Jacobo Bielak, PhD, Professor, Department of Civil and Environmental Engineering,

Carnegie Mellon University

Piervincenzo Rizzo, PhD, Associate Professor, Department of Civil and Environmental

Engineering

Andrew Bunger, PhD, Assistant Professor, Department of Civil and Environmental

Engineering

Dissertation Director: John C. Brigham, PhD, Assistant Professor, Department of Civil

and Environmental Engineering and Bioengineering

COMPUTATIONAL APPROACHES TO EFFICIENTLY MAXIMIZE SOLUTION CAPABILITIES AND QUANTIFY UNCERTAINTY FOR INVERSE PROBLEMS IN MECHANICS

Bahram Notghi, PhD

University of Pittsburgh, 2014

Computational approaches to solve inverse problems can provide generalized frameworks for treating and distinguishing between the various contributions to a system response, while providing physically meaningful solutions that can be applied to predict future behaviors. However, there are several common challenges when using any computational inverse mechanics technique for applications such as material characterization. These challenges are typically connected to the inherent ill-posedness of the inverse problems, which can lead to a nonexistent solution, non-unique solutions, and/or prohibitive computational expense.

Toward reducing the effects of inverse problem ill-posedness and improving the capability to accurately and efficiently estimate inverse problem solutions, a suite of computational tools was developed and evaluated. First, an approach to NDT design to maximize the capabilities to use computational inverse solution techniques for material characterization and damage identification in structural components, and more generally in solid continua, is presented. The approach combines a novel set of objective functions to maximize test sensitivity and simultaneously minimize test information redundancy to determine optimal NDT parameters. The NDT design approach is shown to provide measurement data that leads to consistent and significant improvement in the ability to accurately inversely characterize variations in the Young's modulus distributions for simulated test cases in comparison to alternate NDT designs. Next, an extension of the NDT design approach is presented, which includes a technique to address potential system uncertainty and add robustness to

the resulting NDT design, again in the context of material characterization. The robust NDT design approach uses collocation techniques to approximate the modified objective functionals that not only maximize the test sensitivity and minimize the test information redundancy, but now also maximize the test robustness to system uncertainty. The capability of this probabilistic NDT design method to provide consistent improvement in the ability to accurately inversely characterize variations in the Young's modulus distributions for cases where systems have uncertain parameters, such as uncertain boundary condition features, is again shown with numerically simulated examples. Lastly, an approach is presented to more directly address the computational expense of solving an inverse problem, particularly for those problems with significant system uncertainties. The sparse grid method is used as the foundation of this solution approach to create a computationally efficient polynomial approximation (i.e., surrogate model) of the system response with respect to both deterministic and uncertain parameters to be used in the inverse problem solution process. More importantly, a novel generally applicable algorithm is integrated for adaptive generation of a data ensemble, which is then used to create a reduced-order model (ROM) to estimate the desired system response. In particular, the approach builds the ROM to accurately estimate the system response within the expected range of the deterministic and uncertain parameters, to then be used in place of the traditional full order modeling (i.e., standard finite element analysis) in constructing the surrogate model for the inverse solution procedure. This computationally efficient approach is shown through simulated examples involving both solid mechanics and heat transfer to provide accurate solution estimates to inverse problems for systems represented by stochastic partial differential equations with a fraction of the typical computational cost.

TABLE OF CONTENTS

LIST OF TABLES

LIST OF FIGURES

PREFACE

I would like to express my appreciation and thanks to my advisor Professor John C. Brigham. You have been tremendous mentor for me. In every discussion, his deep insight has helped develop the directions for my research. I would like to thank you for encouraging my research and for allowing me to grow as a researcher.

I would like to thank Professor Jacobo Bielak, Professor Andrew Bunger, and Professor Piervincenzo Rizzo for serving on my graduate committee and for their support throughout my studies.

I also would like to thank my colleagues in Professor John C. Brighm's group for their help and encouragement during my PhD study.

I would like to dedicate this Doctoral dissertation to my parents, Manoochehr Notghi and Farzaneh Sabeti, who raised me with a love of science and supported me in all my pursuits. Finally, I would like to thank my sister, Sepideh, for all her support and encouragement.

1.0   OPTIMAL NONDESTRUCTIVE TEST DESIGN FOR MAXIMUM SENSITIVITY AND MINIMAL REDUNDANCY FOR APPLICATIONS IN MATERIAL CHARACTERIZATION

1.1   ABSTRACT

An approach to nondestructive test (NDT) design for material characterization and damage identification in structural components, and more generally in solid continua, is presented and numerically tested. The proposed NDT design approach is based on maximizing a measure of the sensitivity of the test responses to changes in the material properties of the structure while also maximizing a measure of the difference in the response components. As such, the optimally designed NDT provides significant improvement in the the ability to solve subsequent inverse characterization problems by extracting the maximum amount of non-redundant information from the system to increase the inverse solution observability. The NDT design approach is theoretically able to include any and all possible design aspects, such as the placement of sensors and actuators and determination of actuation frequency, among others. Through simulated test problems based on the characterization of damage in aluminum structural components utilizing steady-state dynamic surface excitation and localized measurements of displacement, the proposed NDT design approach is shown to provide NDT designs with significantly higher measurement sensitivity as well as lower information redundancy when compared to alternate test approaches. More importantly, the optimized NDT methods are shown to provide consistent and significant improvement in the ability to accurately inversely characterize variations in the Young's modulus distributions for the simulated test cases considered.

1.2 INTRODUCTION

There has been a substantial amount of work to-date on a variety of computational inverse mechanics approaches for the characterization, design, and/or control of complex systems in several fields of science and engineering [4, 6, 8, 10, 62]. In particular, techniques for inverse characterization of material properties in solids from nondestructive testing (NDT) data are of great significance in areas spanning medicine [2] to structural engineering [35], since material properties provide valuable insight about the health of the system, whether it is tissue or steel. One of the more common computational approaches to solve these inverse characterization problems is to cast them as optimization problems, in which a computational representation (e.g., finite element) is created of the NDT performed, the representation is parameterized with respect to the unknown material properties (to be characterized), and a nonlinear optimization method is employed to determine the estimate of the material parameters that minimizes the difference between the output of the computational representation and the measurements of the NDT. Such computational inverse solution methods are typically generally applicable, providing a means to determine a wide variety of properties from a wide variety of nondestructive testing methods. However, there are several common challenges when using any computational inverse mechanics techniques, typically regarding ill-posedness of the inverse problems, which can lead to a nonexistent solution, nonunique solutions, and/or excessive computational expense for the optimization algorithm [18].

One effective approach to overcome, or at least relieve some of the ill-posedness of nondestructive evaluation (NDE) problems is to address the complementary inverse problem of optimal design of the NDT method. In other words, if the NDT method is controllable or modifiable to any degree, aspects such as the actuation and measurement locations, directions, and frequencies could be identified using the same or similar tools as used for the NDE solution procedure to somehow optimize the solvability/observability of the NDE problem resulting from the NDT method. Moreover, NDT design can be an important step for the feasibility of implementing a particular NDT system by optimizing the amount of resources needed to characterize the system, subject to monetary cost, time, and/or accessibility constraints.

A large amount of focus has been placed in recent years on developing methods for test design, often specifically sensor optimization, for structural health monitoring and NDE approaches One of the most important features of these methods is the metric used to define the quality of a given sensor distribution. The existing methods are diverse and have shown mixed results, including those relying on *ad hoc* approaches such as maximizing the contribution of the sensor locations to the mode shapes of the structure [38], as well as statistical or probabilistic approaches, such as those that minimize the information entropy of the system that corresponds to the uncertainty of the model parameters [64], those that attempt to maximize the probability of detection for the system [11, 32]. The methods to then employ these metrics to improve NDT quality are also varied, including system identification strategies that iteratively discard or include candidate sensors for the NDT to optimally represent the target metrics [74, 43, 44], as well as traditional optimization strategies that create an objective function directly relating to the NDT quality metric and use iterative optimization to minimize or maximize the objective function [68, 91].

In the majority of cases, the existing sensor optimization methods are specialized (i.e. may not be extensible) to the intended quantity to be identified and the nature of the apparatus in which they can be used. Furthermore, the optimization capabilities are typically limited to the number of sensors and their corresponding locations, with little attention paid to actuation location, orientation, and/or excitation frequency and duration. Alternatively, Raich and Liszkai [67] presented a potentially generalizable approach for NDT design that relies on maximizing the total damage sensitivity of the frequency response functions collected by a set of sensors while simultaneously minimizing the number of sensors employed. Although only shown to be applied to frequency response function-based NDE of beam and frame structures, the concept of maximizing sensitivity should theoretically be applicable to a wide range of systems for NDE applications, physical processes, and NDT excitation and sensing options.

The current work presents an approach to extend the concept of maximizing damage sensitivity for optimal NDT design in a generally applicable way for NDE and material characterization problems in continua. Furthermore, the approach presented also incorporates an additional objective to prevent redundancy of the test information to further maximize

the resulting inverse solution capabilities for the designed NDT. In the following section a general inverse characterization solution framework is outlined. Then, the method for optimal NDT design to maximize inverse characterization solution capability is presented. Lastly, simulated examples relating to characterization of semi-localized variations in the Young's modulus distribution in structures from frequency-response-based NDT are presented, including analysis of the NDT design metrics relating to sensitivity and information redundancy and inverse characterization results, which is followed by the concluding remarks.

1.3 INVERSE PROBLEM FORMULATION AND SOLUTION STRATEGY

Although the concepts presented herein are easily generalizable, which is one of the key proposed benefits, to provide context, the present work focuses on NDE of material properties in structural components using frequency-response-based NDT methods. Potential application of this NDE approach could include detecting damage in manmade structural components, using a common assumption that the type of damage to be identified is manifested in changes to the material properties such as material stiffness [35, 30], or determining disease-related changes in material properties of biological structures [3]. As such, for a given NDT the inverse characterization solution approach (depending on implementation and application also referred to as model updating or by other monikers) can be cast as an optimization problem to minimize an objective functional that quantifies the difference between the experimental measurements for the structure and those predicted numerically, such as

$$J(E(\vec{x})) = \left\| \frac{R^{ndt}(\vec{\gamma}_k) - R^{sim}(\vec{\gamma}_k, E(\vec{x}))}{R^{ndt}(\vec{\gamma}_k)} \right\|_k, \tag{1.1}$$

where $E(\vec{x})$ is the material property (e.g., Young's modulus) distribution to be determined, $\vec{x} \in \Omega$ is the spatial position vector in the domain of the structure Ω, R^{ndt} is the measured response of the structure for the NDT, R^{sim} is the simulated estimate to the structure's response from the NDT for a given material property estimate, $\{\vec{\gamma}_k\}_{k=1}^{N_T}$ is the set of all NDT combinations (e.g., excitation frequency, sensor location, actuator location, orientation

of sensors etc.), assuming the NDT produces a set of discrete measurements with a total number of NDT measurement combinations of N_T, and $\|.\|_k$ is some suitable metric norm that combines the contributions of each measurement to produce the total error functional J.

Commonly, approaches for computational inverse mechanics will rely on the traditional numerical analysis tools such as finite element or boundary element methods to produce the simulated estimates of the structure's response from the NDT (often referred to as solving the "forward problem"), with the finite element method used for the examples herein [34, 56]. Of critical importance to the inverse procedure is that the computational forward modeling both accurately and efficiently represents the true physical behavior of the system. Without accurate representation, an inverse solution may be unattainable, or worse yet, any apparent solution may be dramatically incorrect. Yet, the typical practical limitation in the application of the inverse approaches is the computational expense associated with this numerical modeling of the system to be evaluated. Similarly, it is important that the nonlinear optimization applied to minimize the objective functional shown in 1.1 is able to traverse the optimization search space, which is typically significantly non-convex, both efficiently and consistently to accurately estimate the unknown properties of the structure. Potential optimization techniques are generally lumped into two categories: gradient-based [59, 54] and non-gradient-based [21, 37, 76], with each having certain benefits and shortcomings. For instance, gradient-based methods typically converge to a solution estimate in relatively few iterations, but are susceptible to convergence to local (i.e., inaccurate) solutions if initialized far from the global solution. In contrast, non-gradient-based methods are generally more capable of consistently identifying global solutions, but typically require significantly more iterations (i.e., evaluations of the simulated structural response) than gradient-based methods, which can become computationally prohibitive. For instance, for just the single example computational inverse mechanics application of damage identification/characterization, several examples exist in the literature for a variety of structure types with a variety of optimization approaches utilized (gradient, non-gradient, heuristic, etc.) [81, 26, 48, 16].

However, regardless of the optimization method, it is critically important that the error functional 1.1, and therefore the measured response of the structure for the chosen NDT is sensitive to changes in the material properties to be determined ($E(\vec{x})$) if the search process is expected to identify an accurate inverse approximation. For gradient-based methods, the sensitivity obviously directly affects the search process in that the gradient of the error functional with respect to the unknown properties drives the search direction and magnitude. Moreover, although non-gradient-based methods do not directly rely on the sensitivity to drive the search, there is still a universal need to have an objective functional that varies significantly (i.e., is sensitive) with respect to the unknown properties throughout the search space to provide information that ultimately directs the optimization towards a solution, if nothing else, to maintain an efficient and consistent search process.

1.4   OPTIMAL DESIGN FOR NON DESTRUCTIVE TEST

Based on the observation that response sensitivity is critical to inverse solution capability, a natural hypothesis is that choosing the NDT that somehow maximizes the sensitivity of the response measurements with respect to changes in the unknown properties will maximize the capability to then inversely characterize the material properties with that NDT. An example of this concept of maximizing sensitivity for optimal NDT was recently employed by Raich and Liszkai [67], in which sensor and excitation locations were determined that maximized the cumulative sensitivity of the responses with respect to damage to all structural elements to design frequency response function-based NDT for beam and frame structures. Similarly to this previous work, in a general sense, the complementary inverse problem of designing the optimal NDT can be cast as an optimization problem to maximize a functional that quantifies the change in the measured response with respect to the unknown structural properties of the following form

$$P\left(\{\vec{\gamma}_k\}_{k=1}^{N_T}\right) = \left\|D_E R^{sim}(\vec{\gamma}_k, E(\vec{x}))\right\|_{\Omega,k}, \tag{1.2}$$

where $D_E R^{sim}$ is some form of the derivative or the gradient of the response functional with respect to the material properties and $\|.\|$ is now some suitable metric norm that combines the sensitivity contributions of each measurement with respect to the material properties over the entire domain of the structure (Ω) to produce the total sensitivity functional P.

While maximizing the functional shown in 1.2 addresses the sensitivity objective, in the general sense and particularly for cases in which candidate locations of sensors and actuations are continuously (or nearly continuously) distributed throughout the domain of the structures being considered, maximizing P alone may lead to redundant measurement information, and ultimately a poor use of resources. For example, the work by Stephan [78] proposed a method to select sensor locations by maximizing the observability of mode shapes, but showed that it was also necessary to simultaneously minimize the information shared by a collection of sensors, otherwise the sensors would be clustered and not reasonably distributed throughout the structure. Following this concept of reducing shared information, a second functional can be formed that quantifies the similarity of the response measurements in terms of orthogonality (i.e., responses are less similar if they are closer to orthogonal) as

$$\theta_{i,j} = \arccos\left(\frac{\langle R^{sim}(\vec{\gamma}_i, E(\vec{x})), R^{sim}(\vec{\gamma}_j, E(\vec{x}))\rangle}{\|R^{sim}(\vec{\gamma}_i, E(\vec{x}))\| \, \|R^{sim}(\vec{\gamma}_j, E(\vec{x}))\|}\right), \quad \forall \, i,j \in [1, N_T], \ i \neq j \qquad (1.3)$$

where $\langle .,. \rangle$ is a suitable inner product operator (e.g., standard vector dot product if the responses are simply a discrete vector of sensor measurements at a set of excitation frequencies) and $\|.\|$ can be defined as

$$\left\|R^{sim}(\vec{\gamma}_i, E(\vec{x}))\right\|^2 = \langle R^{sim}(\vec{\gamma}_i, E(\vec{x})), R^{sim}(\vec{\gamma}_i, E(\vec{x}))\rangle. \qquad (1.4)$$

As such, the solution of the following multi-objective optimization problem should yield potential designs for NDT aspects, including sensor and actuator locations, orientations,

and frequencies, along with any other conceivable aspect, to produce tests that are maximally sensitive to changes in the material properties to be determined and simultaneously minimally redundant

$$\underset{\{\vec{\gamma}_k\}_{k=1}^{N_T}}{\text{Maximize}} \quad \begin{cases} P\left(\{\vec{\gamma}_k\}_{k=1}^{N_T}\right) \\ \underset{\substack{i,j\in[1,N_T] \\ i\neq j}}{\text{Minimum}} \;\; \theta_{i,j} \end{cases} . \tag{1.5}$$

Note that maximizing the minimum value of the similarity metric, $\theta_{i,j}$, is equivalent to maximizing the dissimilarity over the entire set of NDT measurement combinations.

A final important point is that the material properties to be determined ($E(\vec{x})$) must be initialized (i.e., set to some chosen value) in order to solve the multi-objective NDT optimization problem in 1.5. There is not necessarily one preferred choice for the initial properties, and these chosen properties will affect the outcome of the NDT design to some degree. However, for many NDE problems some value(s) for initial (i.e., healthy) properties are known or can be assumed within a reasonable accuracy for the structure. Furthermore, many applications seek to determine relatively subtle deviations of the structural properties from this healthy state (e.g., structural damage detection), and therefore, utilizing these initial healthy structural properties for the solution of the NDT optimal design problem outlined above can be a natural selection.

1.5   EXAMPLES AND DISCUSSION

To display the potential capabilities and challenges of the approach presented for optimizing the NDT through maximization of sensitivity and minimization of redundancy for improved inverse material characterization capabilities, two simulated case studies were considered regarding characterization of material stiffness distribution in aluminum structures as could be related to possible damage. The first problem consisted of a simulated cantilever beam with an unknown distribution of stiffness along the length of the beam, while the second problem consisted of a simulated plate structure with unknown semi-localized reductions in stiffness throughout the plate domain. In both case studies the NDT was first designed

using the proposed optimization strategies and compared to select design alternatives. Then the characterization problem was solved with the optimally designed NDT as well as the design alternatives using a fixed number of finite element analyses for each trial to test the potential performance improvement due to the NDT design optimization strategy. Due to the stochastic nature of the optimization inverse solution strategy, the inverse characterization solution procedure was repeated five times for every trial of each NDT case to quantify the accuracy and consistency of the methods.

1.5.1   Nondestructive Testing and Forward Problem

As discussed previously, although the concepts presented are generally applicable, for context the examples considered herein consist of structures tested with frequency-response-based NDT. Directly measuring the frequency response (e.g., displacements, accelerations, etc.) of a structure can provide substantial information for the resulting NDE problem, while also relieving the need for intermediate processing steps required by alternate methods such as modal analysis approaches [57]. Specifically for the examples herein, the NDT consisted of a localized harmonic actuation applied to the surface of the structure over a range of frequencies and with the resulting steady-state harmonic displacement amplitude measured with a set of discrete sensors for each actuation frequency. Displacement measurement was chosen solely based upon simplicity of implementation, and although not a particularly common approach, displacement measurement could be acquired with techniques similar to those shown in [75, 90]. As such, the potential NDT design parameters included the set of actuation frequencies, $\{\omega_k\}_{k=1}^{N_w}$, the actuation location (assuming the force acts normal to the surface), $\vec{X}_F$, the set of sensor locations, $\left\{\vec{X}_{Sk}\right\}_{k=1}^{N_s}$, and the set of corresponding sensor orientations, $\{\alpha_k\}_{k=1}^{N_S}$.

For simplicity the actuation was assumed to be reasonably represented by an applied harmonic pressure force to the surface of the structure being analyzed. For both generating the experimental data and simulating the forward problem during the inverse solution process the structures were assumed to behave linearly with respect to the NDT described, and therefore be defined by steady-state dynamic solid mechanics and analyzed using the finite

element method. The healthy (i.e., undamaged) material parameters were assumed to be defined by a Young's modulus of $E_H = 69GPa$, a Poison's ratio of $\nu = 0.3$, and a density of $\rho = 2700kg/m^3$. The damage to be characterized was assumed to be manifested as a reduction in the Young's modulus, while all other material properties remained constant (note that Young's modulus reduction for approximating the effects of damage in solids and structures has been previously utilized in a variety of applications [27, 50, 5, 24, 29]). To reduce the computational expense, both case studies considered relatively thin structures that were excited and responses measured in plane so that the plane stress assumption could be employed and the simulations reduced to two-dimensions. Lastly, to add realism to the simulated examples and to partially relieve the inverse crime inherent in simulated experiments, 1% Gaussian white noise was added to all responses for the simulated NDT prior to applying the inverse characterization procedure as

$$R^{ndt} = R_0^{ndt}(1 + 0.01\aleph) \, , \tag{1.6}$$

where R_0^{ndt} is the original simulated test response without noise and $\aleph$ is a normally distributed random variable with zero mean and unit variance.

For implementation of the NDT optimization procedure (as described by 1.5), the domains of each structure were discretized into elements, the beam only along its length and the plate along its height and width, and the Young's modulus of the jth element labeled as $E(\vec{x}_j)$. Although arbitrary, the size of the elements was taken to approximately match the size of the converged discretization (i.e., finite element mesh) used to accurately simulate the forward problems (although only one direction was discretized for the Young's modulus of the beam in contrast to the two-dimensional elements of the forward problem). In addition, for simplicity, finite difference was used to calculate the change in the measured response with respect to the Young's modulus at an element. Thus, a discretized form of the sensitivity metric 1.2 could be defined as

$$P = \sum_{i=1}^{N_w} \sum_{j=1}^{N_S} \sum_{k=1}^{N_e} S_{ijk} \, , \tag{1.7}$$

with

$$S_{ijk} = \left| \frac{R^{sim}(\omega_i, \vec{X}_{Sj}, \alpha_j, \vec{X}_F, E_H) - R^{sim}(\omega_i, \vec{X}_{Sj}, \alpha_j, \vec{X}_F, E_{Dk})}{\frac{1}{2}\left(R^{sim}(\omega_i, \vec{X}_{Sj}, \alpha_j, \vec{X}_F, E_H) + R^{sim}(\omega_i, \vec{X}_{Sj}, \alpha_j, \vec{X}_F, E_{Dk})\right)\Delta E} \right| , \qquad (1.8)$$

where N_e is the total number of elements used for the discretization of Young's modulus, $|.|$ is the absolute value, E_H is the initial (healthy) Young's modulus distribution, and E_{Dk} is the Young's modulus distribution with the Young's modulus of the kth element reduced by a fixed Young's modulus perturbation value of ΔE. Lastly, the discretized form of the measurement similarity metric, which was particularly focused on ensuring diversity in the sensor locations, was defined as shown in 1.3 and 1.4 with

$$\langle R^{sim}(\vec{\gamma}_i), R^{sim}(\vec{\gamma}_j) \rangle = \sum_{k=1}^{N_w} R^{sim}(\omega_k, \vec{X}_{Si}, \alpha_i, \vec{X}_F, E_H) \cdot R^{sim}(\omega_k, \vec{X}_{Sj}, \alpha_j, \vec{X}_F, E_H) , \qquad (1.9)$$

In general, the solution to the multi-objective optimization problem outlined by 1.5 can be described by a set of non-dominated solutions with respect to both objectives (i.e., Pareto front). Therefore, a criteria is needed for selecting the one solution from the Pareto front that will be implemented as the optimal NDT. For the present work the one solution for the NDT design was selected using the "nearest to ideal point" method. The nearest to ideal point method selects the point that has the minimum euclidean distance to an imaginary "ideal point", which has the optimal value for each objective function separately [46, 45].

1.5.2 Inverse Characterization Problem

Once the NDT was designed, test distributions of Young's modulus were selected and simulated experimental test measurements were generated, including the artificial noise discussed. Then, the computational inverse solution approach discussed in Section 1.3 was applied to estimate the Young's modulus distribution as if it were unknown, and thus, the capability to accurately solve the inverse characterization problem for the chosen NDT was quantified. In

11

particular, for the examples presented, the objective functional employed to measure the difference between the "experimental" measurements and those predicted by the optimization simulations was defined as

$$J = \frac{1}{N_w N_S} \sum_{k=1}^{N_w} \sum_{i=1}^{N_S} \left| \frac{R^{ndt}(\omega_k, \vec{X}_{Si}, \alpha_i, \vec{X}_F) - R^{sim}(\omega_k, \vec{X}_{Si}, \alpha_i, \vec{X}_F, E(\vec{x}))}{R^{ndt}(\omega_k, \vec{X}_{Si}, \alpha_i, \vec{X}_F)} \right| . \tag{1.10}$$

Lastly, the surrogate-model accelerated random search (SMARS) optimization algorithm [18] was applied to identify the Young's modulus distribution that minimizes 1.10, and therefore, estimate the solution to the inverse characterization problem. The SMARS algorithm iteratively combines the global random search algorithm with a locally applied surrogate model method, and provides an optimization technique that maintains global search capabilities over relatively large parameter domains while having a relatively low computational expense.

1.5.3   Example 1 - Beam

The first case study considered a $1m \times 0.2m \times 0.02m$ aluminum cantilever beam, and the damage (i.e., change in Young's modulus) to be inversely determined by the NDT was assumed to solely vary along the length of the beam and be constant in the cross-sectional directions. The beam was modeled as a continuum and taken to be fixed along the left boundary and free to displace along the other three boundaries. The simulated NDT consisted of applying a $1kPa$ harmonic load to a $5cm$ region normal to the top surface at the top right corner of the beam. For simplicity and based on preliminary analysis of the problem, two displacement sensors were determined to be sufficient and their potential locations were restricted to the top surface of the beam between $0.03m$ to $0.97m$ (note that the number of sensors could also easily be added as an unknown for the NDT optimization approach presented). In addition, the potential excitation frequencies of the NDT were assumed to be between $100Hz$ to $1000Hz$ and be restricted to three evenly spaced values. Therefore, the unknown NDT parameters to be determined were the longitudinal location of each of the two displacement sensors and the minimum and maximum excitation frequencies.
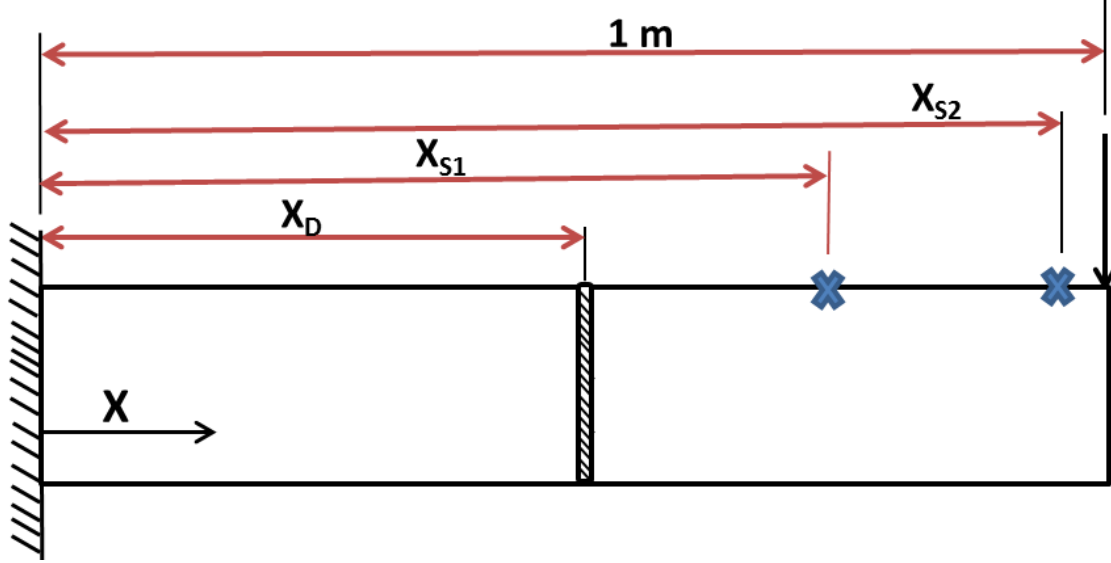
Figure 1.1: Schematic for Example 1 - Beam, displaying the sensor locations, X_{Si}, obtained by optimizing the NDT with the method presented and the selected "experimental" damage location, X_D, to be approximated by the inverse characterization process.

Through the application of the presented approach for maximizing the test sensitivity and minimizing the information redundancy the optimal NDT parameters for the sensor locations and actuation frequency were determined to be: $X_{S1} = 0.81m$, $X_{S2} = 0.94m$, $\omega_{min} = 700Hz$, and $\omega_{max} = 1000Hz$. Figure 1.1 shows a schematic of the beam example, with the approximate sensor locations indicated as obtained from the method presented for NDT optimization. For comparison, the NDT design process was performed a second time only considering the sensitivity objective (the first objective in 1.5) and neglecting the redundancy objective (the second objective in 1.5), which is an approach more closely related to the previous sensitivity maximization technique presented in [67], and referred to herein as the "Single-Objective" NDT design. The Single-Objective NDT design produced NDT parameters of: $X_{S1} = 0.81m$, $X_{S2} = 0.72m$, $\omega_{min} = 700Hz$, and $\omega_{max} = 1000Hz$. Table 1.1 shows the values of the sensitivity metric and the similarity metric (even though it was not an objective of the Single-Objective NDT design) corresponding to the two NDT design cases considered. For both the Optimal (two-objective) and the Single-Objective NDT designs the

Table 1.1: Values of the sensitivity metric (the first objective in 1.5) and the redundancy metric (the second objective in 1.5) for the Optimal NDT design and Single-Objective NDT design for Example 1 - Beam.

NDT Design Case	Sensitivity Metric	Redundancy Metric
Optimal	1.21	89°
Single-Objective	2.09	71°

sensors were determined to be located near to the free end of the cantilever beam, which could be expected simply due to the significantly higher response magnitude away from the beam support. Of particular note is that the excitation frequency range and the first sensor location were identical for both NDT design cases. This result would seem to imply that this first sensor and frequency range contribute maximally to the sensitivity of the NDT within the search ranges considered. Alternatively, the second sensor location was considerably different for the two NDT design cases, which combined with Table 1.1, indicates that the sensor location of $0.72m$ is considerably more sensitive to Young's modulus variations, but is also significantly more redundant in terms of the information content when combined with the first location of $0.81m$ compared to the second sensor location of $0.94m$ obtained with the two-objective strategy presented.

To quantify the efficacy of the two NDT design results, a subsequent series of inverse characterization tests were performed with both sets of NDT design parameters applied in turn. For increased efficiency and simplicity of the presentation and interpretation, the inverse characterization process assumed that the size of the damaged region on the beam was known (i.e., given) as a value of $0.025m$. In other words, the inverse characterization sought the location, X_D, and magnitude in terms of the Young's modulus percent reduction, D, of a region of damage initiation of a predicable small size, such that $E(X_D) = (1 - D) \cdot E_H$. The remainder of the beam (i.e., undamaged portion) had a constant Young's modulus value of E_H. For the characterization solution process the damage location was assumed

to be between $0m$ to $1m$, and the damage magnitude was assumed to be between 0 to 1. The stopping criteria was set to a maximum of 1500 finite element analyses for the SMARS optimization process to estimate the damage parameters for all inverse characterization trials with each of the NDT designs.

First, to show the consistency of the characterization results, regardless of the stochastic nature of the optimization algorithm which was used to solve the characterization problem, five trials of the the inverse characterization process were performed for one damage scenario. For this first test, the simulated experimental data was generated with the damage location arbitrarily taken to be $X_D = 0.5m$ and the damage magnitude was taken to be $D = 0.8$. Table 1.2 shows the mean and standard deviation of the specified NDT displacement sensor measurement errors, calculated as shown in 1.10, produced by the solutions obtained from the five trials of the inverse characterization process for each NDT design. More importantly, Table 1.2 also shows the target values for the unknown material parameters (i.e., values used to generate the simulated experimental data) and the mean and standard deviation of the material parameter values obtained from the five trials of the inverse characterization process for each NDT design. Then, to show the capabilities of the NDT design results to characterize a variety of damage scenarios, five additional trials of the inverse characterization process were performed, each with a different randomly-generated set of damage parameters. Table 1.3 shows the estimated values as well as the mean and standard deviation of the relative l_2-Error for the damage parameters (i.e., location and magnitude) obtained from a single inverse characterization process for each NDT design with respect to the five randomly generated target values.

Overall, the characterization results show a clear improvement in the inverse characterization capabilities for the Optimal NDT design that simultaneously maximized the test sensitivity to material variations and the dissimilarity in the sensor measurement information in comparison to the Single-Objective NDT design that only maximized the test sensitivity. Although difficult to make direct comparisons, the measurement error for the Optimal design was consistently minimized to a level that was two orders of magnitude lower than that for the Single-Objective design. When noting that the sensor measurements for the two tests were similar in magnitude, the measurement error results indicate that the Optimal NDT

Table 1.2: Target (i.e., simulated experimental) values for the unknown percent reduction in elastic modulus (D) and the location of the center of the elastic modulus reduction (X_D), the mean and standard deviation of the unknown values as estimated by the inverse characterization process for all five trials with both the Optimal NDT design and the Single-Objective NDT design, and the mean and standard deviation of the corresponding displacement sensor measurement error (J) for Example 1 - Beam.

	D	X_D	J
Target Value	0.80	0.50	-
Optimal NDT Design			
Mean	0.801	0.507	0.0007
Std. Dev.	0.003	0.027	0.006
Single-Objective NDT Design			
Mean	0.924	0.620	0.13
Std. Dev.	0.08	0.190	0.085

Table 1.3: Five randomly-generated target (i.e., simulated experimental) damage parameters and the corresponding parameters estimated by the inverse characterization process with both the Optimal NDT design (Optimal) and the Single-Objective NDT design (Single-Obj.) and the resulting relative l_2-Error in the damage parameter solutions as well as the mean and standard deviation over all five trials for Example 1 - Beam.

Trial		D	X_D	L_2-Error
1	Target Value	0.70	0.20	-
	Optimal	0.71	0.22	0.031
	Single-Obj.	0.43	0.11	0.390
2	Target Value	0.90	0.60	-
	Optimal	0.89	0.64	0.038
	Single-Obj.	0.88	0.58	0.026
3	Target Value	0.60	0.40	-
	Optimal	0.61	0.49	0.126
	Single-Obj.	0.69	0.52	0.208
4	Target Value	0.80	0.80	-
	Optimal	0.86	0.83	0.059
	Single-Obj.	0.88	0.87	0.094
5	Target Value	0.20	0.70	-
	Optimal	0.19	0.71	0.019
	Single-Obj.	0.18	0.68	0.039
Optimal			Mean	0.055
			Std. Dev.	0.042
Single-Obj.			Mean	0.151
			Std. Dev.	0.152

design measurements provided an optimization search space that was significantly easier for the optimization algorithm to traverse than in the cases for the Single-Objective design. More importantly, the material parameters obtained from inverse characterization with the Optimal NDT design were nearly exact for all trials comparing with the target values, displaying the capability of the design approach presented herein to provide an NDT method with sufficient information to accurately characterize the material properties of a structure. In contrast, the material parameters obtained with the Single-Objective NDT design had errors in the range of 15% on average (nearly three times that for the Optimal NDT design), which displays the importance of including the second objective in the NDT design process and maintain diversity in the sensor measurement information.

1.5.4 Example 2 - Plate

To examine the capability of the NDT design approach presented to generalize to other similar NDE problems, the second case study considered a $1m \times 1m \times 0.02m$ aluminum plate, with the NDE objective of determining a semi-localized change in the Young's modulus distribution throughout the plate (again, as could be representative of a damage scenario). The plate was assumed to be fixed along the bottom boundary and free to displace along the other three boundaries. The simulated NDT consisted of applying a $1kPa$ harmonic load to a $5cm$ region normal to the top surface of the plate, which was restricted to 4 discrete potential (i.e., to be designed) locations: $X_F = 0m$, $X_F = 0.25m$, $X_F = 0.5m$, or $X_F = 0.75m$, as shown in the schematic in Figure 1.2. Note that the potential actuation locations were chosen arbitrarily, as could be the case in practice where external restrictions could produce limitations on actuation locations, and all produce an unsymmetric deformation. Again for simplicity and based on preliminary analysis of the problem, four displacement sensors were determined to be sufficient, and the potential horizontal and vertical coordinates of the sensor locations were restricted to $X_{Si} \in [0, 1m]$ and $Y_{Si} \in [0.02m, 0.98m]$, respectively, to avoid placing a sensor at the support condition or on the surface where the actuation force was
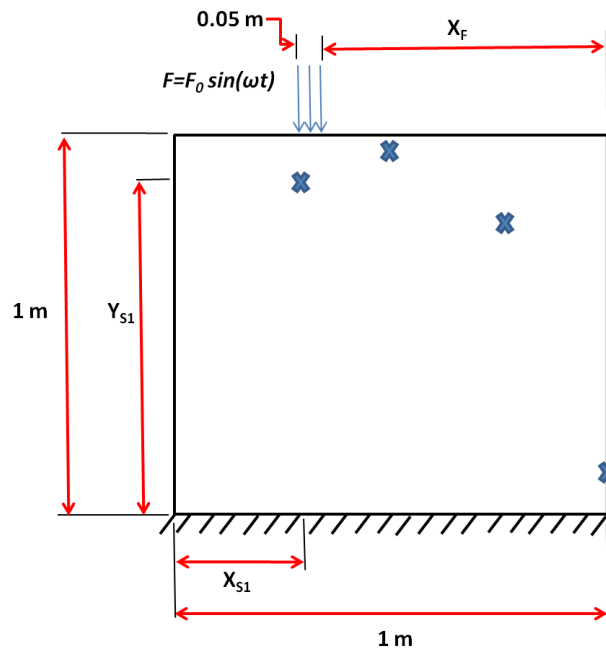
Figure 1.2: Schematic for Example 2 - Plate, displaying the sensor locations, X_{Si} and Y_{Si}, and the actuator location, X_F, to be determined by optimizing the NDT with the method presented.

applied. In addition, for this second example the sensor orientation was assumed to be a component in the NDT design optimization, and the sensors were assumed to be potentially oriented to measure either the horizontal or vertical displacement. Lastly, the excitation frequencies of the NDT were assumed to be given as six evenly spaced values from $500Hz$ to $1500Hz$. Therefore, the unknown NDT parameters to be determined were the horizontal and vertical coordinates and the orientation of the four sensors and the horizontal location of the actuation.

As previously, through the application of the presented approach for maximizing the test sensitivity and minimizing the information redundancy the optimal NDT parameters for the sensor and actuator locations were determined to be: $X_{S1} = 0.7m$, $Y_{S1} = 0.75m$, $X_{S2} = 1m$, $Y_{S2} = 0.1m$, $X_{S3} = 0.375m$, $Y_{S3} = 0.85m$, $X_{S4} = 0.55m$, $Y_{S4} = 0.95m$, and $X_F = 0.25m$. All of the sensors were determined to be optimally oriented vertically. To again have a point of comparison, a "Single-Objective" NDT design was created as was done for the previous example (considering only the sensitivity objective), which yielded sensor and actuator locations of: $X_{S1} = 0.34m$, $Y_{S1} = 0.1m$, $X_{S2} = 1m$, $Y_{S2} = 0.1m$, $X_{S3} = 0.42m$, $Y_{S3} = 0.92m$, $X_{S4} = 0.55m$, $Y_{S4} = 0.94m$, and $X_F = 0.25m$. Similarly, all of the sensors were determined to be optimally oriented vertically. Additionally, a third intuitive "Control" NDT design was also utilized for this second example with the same actuation location and sensor orientation as the optimized NDT design, but with the sensors predefined to be located uniformly throughout the plate (as might be done in practice [39]) with: $X_{S1}^{C} = 0.25m$, $Y_{S1}^{C} = 0.25m$, $X_{S2}^{C} = 0.25m$, $Y_{S2}^{C} = 0.75m$, $X_{S3}^{C} = 0.75m$, $Y_{S3}^{C} = 0.25m$, $X_{S4}^{C} = 0.75m$, and $Y_{S4}^{C} = 0.75m$.

Figure 1.3 shows a schematic of the sensor and actuator layouts of the Control NDT design, the Single-objective NDT design, and the Optimal NDT design obtained from the presented approach. Additionally, Table 1.4 shows the values of the sensitivity metric and the similarity metric corresponding to the three NDT design cases considered for this second example. As is not unexpected, the sensitivity metric was increased (i.e., improved) by several orders of magnitude through both optimized NDT approaches in comparison to the Control design, even with the only difference between the tests being the sensor locations.
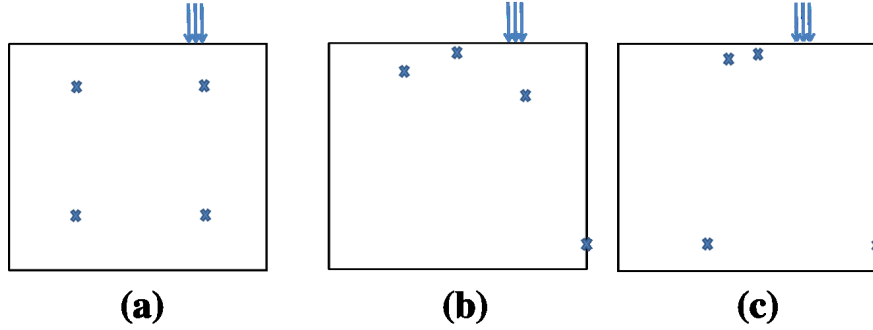
Figure 1.3: Schematics of the NDT designs, including (a) the uniformly distributed sensor locations utilized for the Control NDT design, (b) the sensor locations determined for the Optimal design through the method presented, and (c) the sensor locations determined for the Single-Objective design.

Table 1.4: Values of the sensitivity metric (the first objective in 1.5) and the redundancy metric (the second objective in 1.5) for the Optimal NDT design, the Control NDT design, and the Single-Objective NDT design for Example 2 - Plate.

NDT Design Case	Sensitivity Metric	Redundancy Metric
Optimal	2.26×10^{12}	90°
Control	3.81×10^{7}	0.02°
Single-Objective	2.43×10^{12}	15°

Furthermore, both optimized NDT approaches produced improvements to the redundancy metric in comparison to the Control design, but the Optimal NDT design obtained from the presented approach produced a redundancy metric that was substantially improved in comparison to both the Single-Objective optimal design and the Control design.

To again measure the resulting characterization capability of the optimal NDT design approach, a series of simulated tests were performed with various distributions of Young's modulus throughout the plate to be inversely characterized, and all three (Optimal, Single-Objective, and Control) NDT design were utilized, in turn, to inversely estimate the selected modulus distributions. For all tests in this second example, the Young's modulus distribution was assumed to vary due to semi-localized changes defined by a radial basis function (RBF) representation as

$$E(\vec{x}) = E_H \left[1 - \sum_{i=1}^{N_D} D_i \cdot \exp\left(-\frac{\|\vec{x} - \vec{\epsilon}_i\|^2}{c_i} \right) \right], \tag{1.11}$$

where $\|.\|$ represents the standard l_2-norm. For simplicity, the number of RBFs, N_D, necessary to describe the Young's modulus distribution was assumed to be known for the examples herein. Therefore, the material parameters to be determined by the inverse characterization process were the Young's modulus percent reduction corresponding to each RBF, D_i, the center of each RBF, $\vec{\epsilon}_i$, and the breadth of each RBF, c_i. Two cases of Young's modulus distribution were considered for testing the inverse characterization capabilities of the two NDT designs: a single RBF (i.e., one damage location) and two RBFs (i.e., two damage locations). For the characterization solution process for all tests the material parameters were assumed to be bounded as follows: $D_i \in [0, 1]$, $\vec{\epsilon}_i \in [0, 1] \times [0, 1]$, and $c_i \in [0, 0.1]$. The stopping criteria for the SMARS optimization process to estimate the material (i.e., damage) parameters for the inverse characterization trials for this second example was set to a maximum of 5500 finite element analyses for all tests with one RBF and 6000 finite element analyses for all tests with two RBFs. As before, to show the consistency of the characterization results, regardless of the stochastic nature of the SMARS optimization algorithm, for the first tests five trials of the inverse characterization process were performed each for two damage parameter scenarios, one scenario with a single RBF and one scenario with two RBFs. Then, to show the generalization capabilities a second set of tests were performed

with five additional trials of the inverse characterization for the single RBF scenario and for the two RBFs scenario (i.e., 10 total additional trials), with each trial having a different randomly-generated set of material parameters.

Table 1.5 shows the RBF parameters used to simulate the first set of sensor measurement data for the Optimal, Single-Objective, and Control NDT designs for the single RBF example, the respective means and standard deviations of the inversely estimated RBF parameters over of the five trials for each method for this one damage parameter scenario, as well as the corresponding means and standard deviations of the sensor measurement errors, calculated as shown in 1.10. More importantly, Table 1.6 shows the means and standard deviations for the relative L_2-Error and the relative L_∞-Error for the Young's modulus distributions obtained from the inverse characterization process with respect to the one target Young's modulus distribution and Figure 1.4 shows representative examples (i.e., one result from the five trials) for the Young's modulus distributions corresponding to the Optimal, Single-Objective, and Control NDT designs in comparison to the target distribution. Lastly, Table 1.7 shows the estimated damage parameter values as well as the mean and standard deviation of the relative L_2-Error and the relative L_∞-Error for the Young's modulus distributions obtained from a single inverse characterization process for each NDT design with respect to the five randomly generated target distributions.

Similarly to what was seen in the first example, the resulting estimates of the material properties obtained from the Optimal NDT design were significantly and consistently more accurate than those obtained from both the Control and Single-Objective NDT designs. Although relatively accurate estimates to the material properties were obtained for all trials with all three NDT designs, the Optimal NDT design estimated the Young's modulus distribution in the plate with nearly half or less of the error on average compared to the Control and Single-Objective NDT designs. Furthermore, while all test methods underestimated the damage magnitude (i.e., reduction in Young's modulus), particularly the Optimal and Control designs, the Optimal NDT design estimated the location of the modulus variation (i.e., center of the RBF) nearly identically for all trials in comparison to the results for the Control and Single-Objective NDT designs. What is particularly interesting for the representative case shown (Figure 1.4) is that even though the Control NDT design had a sensor

Table 1.5: Target (i.e., simulated experimental) values for the unknown damage amplitude (D_1), the breadth of the damage region (c_1), and the horizontal and vertical location of the center of the damage region ($\epsilon_1^x, \epsilon_1^y$), the mean and standard deviation of the unknown values as estimated by the inverse characterization process for all five trials with the Optimal NDT design, the Single-Objective NDT design, and the Control NDT design, and the mean and standard deviation of the corresponding displacement sensor measurement error (J) for Example 2 - Plate with a single damage location.

	D_1	c_1	ϵ_1^x	ϵ_1^y	J
Target Value	0.80	0.003	0.400	0.400	-
Optimal NDT Design					
Mean	0.37	0.015	0.400	0.415	0.004
Std. Dev.	0.25	0.013	0.006	0.009	0.003
Single-Objective NDT Design					
Mean	0.79	0.014	0.242	0.224	1.390
Std. Dev.	0.001	0.006	0.212	0.213	2.212
Control NDT Design					
Mean	0.50	0.011	0.423	0.326	0.028
Std. Dev.	0.39	0.009	0.055	0.185	0.034

Table 1.6: Mean and standard deviation of the relative L_2-Error and the relative L_∞-Error of the Young's modulus distribution with respect to the single target (i.e., simulated experimental) distribution for the distributions estimated by the inverse characterization process for all five trials with the Optimal NDT design, the Single-Objective NDT design, and the Control NDT design for Example 2 - Plate with a single damage location.

	L_2-Error	L_∞-Error
Optimal NDT Design		
Mean	0.029	0.104
Std. Dev.	0.016	0.031
Single-Objective NDT Design		
Mean	0.110	0.796
Std. Dev.	0.016	0.006
Control NDT Design		
Mean	0.061	0.477
Std. Dev.	0.017	0.390

Figure 1.4: (a) Target (i.e., simulated experimental) spatial distribution of the Young's modulus and representative examples of the Young's modulus distributions estimated by the inverse characterization process with (b) the Optimal NDT design, (c) the Control NDT design, and (d) the Single-Objective NDT design for Example 2 - Plate with a single damage location (color contours are in units of GPa).

that was significantly more closely placed to the damage location, the improved sensitivity and diversity of the measurements in the Optimal NDT design lead to significantly improved inverse characterization of the material distribution in comparison to a design with the sensors uniformly distributed that would intuitively imply better "coverage" for the inverse characterization problem.

Regarding the final set of analyses involving the plate example with two damage locations, Table 1.8 shows the RBF parameters used to simulate the first set of sensor measurement data, the respective means and standard deviations of the inversely estimated RBF parameters over the five trials for this one damage parameter scenario, and the corresponding means and standard deviations of the sensor measurement errors. In addition, Table 1.9 shows the mean and standard deviations for the relative L_2-Error and the relative L_∞-Error for the Young's modulus distributions obtained from the inverse characterization processes with respect to the one target Young's modulus distribution and Figure 1.5 shows representative examples of the Young's modulus distributions from the five trials corresponding to the Optimal, Single-Objective, and Control NDT designs in comparison to the one target

Table 1.7: Five randomly-generated target values for the unknown damage parameters D_1,c_1, and ϵ_1^x, ϵ_1^y and the corresponding values estimated by the inverse characterization process with the Optimal NDT design (Optimal), the Single-Objective NDT design (Single-Obj.), and the Control NDT design (Control) and the resulting relative L_2-Error and the relative L_∞-Error of the estimated Young's modulus distributions as well as the mean and standard deviation over all five trials with a single damage location.

Trial		D_1	c_1	ϵ_1^x	ϵ_1^y	L_2-Error	L_∞-Error
1	Target	0.600	0.008	0.700	0.800	-	-
	Optimal	0.598	0.023	0.740	0.788	0.071	0.361
	Single-Obj.	0.800	0.002	0.793	0.970	0.080	0.795
	Control	0.595	0.028	0.554	0.698	0.121	0.586
2	Target	0.900	0.010	0.800	0.200	-	-
	Optimal	0.958	0.010	0.865	0.174	0.078	0.545
	Single-Obj.	0.227	0.021	1.000	0.182	0.108	0.211
	Control	0.900	0.027	0.760	0.045	0.139	0.852
3	Target	0.600	0.005	0.200	0.300	-	-
	Optimal	0.101	0.029	0.200	0.278	0.041	0.051
	Single-Obj.	0.843	0.030	0.022	0.355	0.134	0.842
	Control	0.921	0.012	0.199	0.251	0.090	0.685
4	Target	0.700	0.004	0.800	0.700	-	-
	Optimal	0.548	0.003	0.727	0.694	0.051	0.408
	Single-Obj.	0.424	0.018	0.954	0.680	0.070	0.422
	Control	0.771	0.007	0.740	0.823	0.091	0.765
5	Target	0.800	0.009	0.600	0.200	-	-
	Optimal	0.118	0.005	0.739	0.254	0.095	0.077
	Single-Obj.	0.990	0.016	1.000	0.500	0.150	0.990
	Control	0.610	0.011	0.500	0.100	0.100	0.545
Optimal					Mean	0.067	0.288
					Std. Dev.	0.021	0.216
Single-Obj.					Mean	0.109	0.654
					Std. Dev.	0.034	0.326
Control					Mean	0.108	0.686
					Std. Dev.	0.021	0.126

Table 1.8: Target (i.e., simulated experimental) values for the unknown damage amplitudes (D_i), the breadths of the damage regions (c_i), and the horizontal and vertical locations of the centers of the damage regions ($\epsilon_i^x, \epsilon_i^y$), the mean and standard deviation of the unknown values as estimated by the inverse characterization process for all five trials with the Optimal NDT design, the Single-Objective NDT design, and the Control NDT design, and the mean and standard deviation of the corresponding displacement sensor measurement error (J) for Example 2 - Plate with two damage locations.

	D_1	c_1	ϵ_1^x	ϵ_1^y	D_2	c_2	ϵ_2^x	ϵ_2^y	J
Target Value	0.80	0.003	0.20	0.20	0.90	0.004	0.20	0.80	-
Optimal NDT Design									
Mean	0.26	0.014	0.18	0.16	0.56	0.012	0.17	0.75	0.03
Std. Dev.	0.085	0.008	0.03	0.04	0.17	0.004	0.12	0.13	0.01
Single-Objective NDT Design									
Mean	0.48	0.009	0.29	0.03	0.82	0.011	0.17	0.62	0.59
Std. Dev.	0.26	0.010	0.07	0.03	0.18	0.005	0.19	0.22	0.49
Control NDT Design									
Mean	0.31	0.013	0.19	0.15	0.75	0.02	0.30	0.89	0.65
Std. Dev.	0.22	0.007	0.06	0.10	0.27	0.005	0.19	0.10	0.59

distribution with two damage locations. Lastly, Table 1.10 shows the estimated damage parameter values as well as the mean and standard deviation of the relative L_2-Error and the relative L_∞-Error for the Young's modulus distributions obtained from a single inverse characterization process for each NDT design with respect to the five randomly generated target distributions with two damage locations.

It is worth noting that the difficultly of the inverse problem in terms of the ability to accurately and efficiently estimate solutions is not linearly proportional to the number of parameters to be determined, and the difficulty for this example with two RBFs is substantially more than for the previous example of only one RBF. As such, even with an increase in the optimization stopping criteria to 6000 finite element analyses, there is still generally a significantly higher solution error for these final tests than for the previous beam and plate examples. However, once more the NDT design that had been optimized for maximum sensitivity and minimum measurement redundancy performed significantly better than both the Single-Objective NDT design that was only optimized for maximum sensitivity and the Control (i.e., uniformly distributed sensor) NDT design for the purpose of inverse material characterization. For instance, the characterization process with the Optimal NDT design was able to minimize the measurement error to a reasonable stopping point of approximately 3% on average, even for this more challenging inverse problem, whereas the same process with the Single-Objective and Control NDT designs clearly became trapped in local minima in the optimization search space with measurement errors in the range of 59% and 65%, respectively, again showing the improvement to the search process through optimization of the NDT design. Thus, the Optimal NDT design produced estimates for the Young's modulus distributions with an increase in accuracy in the range of 40% or more in comparison to both the Single-Objective and Control NDT designs for all trials (i.e., for both the consistency and generalization tests), again with particular improvements in determining the two damage locations.

Table 1.9: Mean and standard deviation of the relative L_2-Error and the relative L_∞-Error of the Young's modulus distribution with respect to the single target (i.e., simulated experimental) distribution for the distributions estimated by the inverse characterization process for all five trials with the Optimal NDT design, the Single-Objective NDT Design, and the Control NDT design for Example 2 - Plate with two damage locations.

	L_2-Error	L_∞-Error
Optimal NDT Design		
Mean	0.09	0.42
Std. Dev.	0.017	0.15
Single-Objective NDT Design		
Mean	0.14	0.84
Std. Dev.	0.016	0.12
Control NDT Design		
Mean	0.15	0.79
Std. Dev.	0.037	0.19

(a)   (b)   (c)   (d)

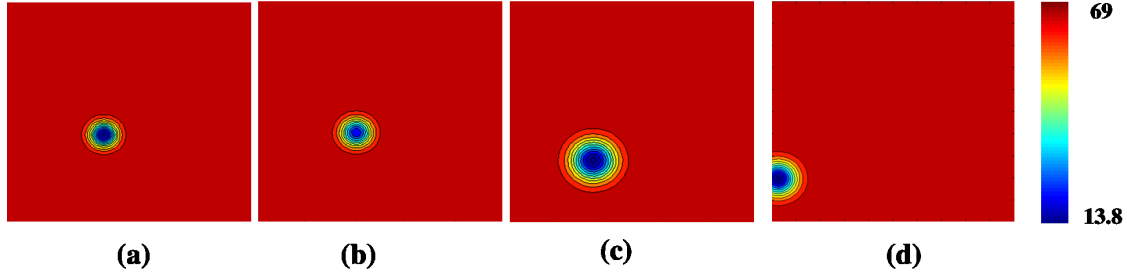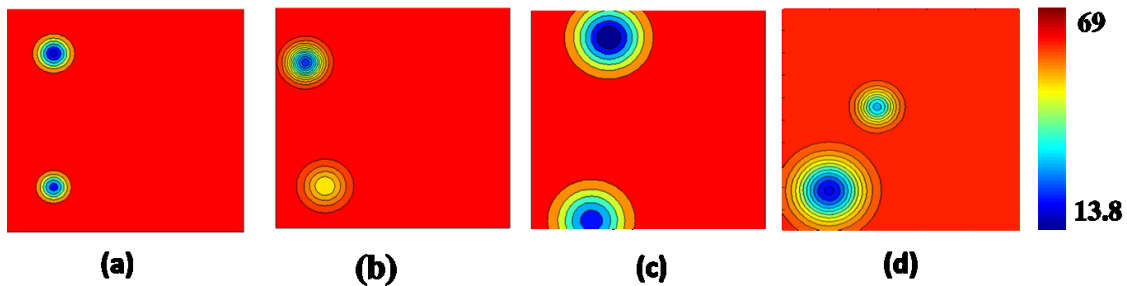Figure 1.5: (a) Target (i.e., simulated experimental) spatial distribution of the Young's modulus and representative examples of the Young's modulus distributions estimated by the inverse characterization process with (b) the Optimal NDT design, (c) the Control NDT design, and (d) the Single-Objective NDT design for Example 2 - Plate with two damage locations (color contours are in units of GPa).

Table 1.10: Five randomly-generated target (i.e., simulated experimental) values for the unknown damage amplitudes (D_i), the breadths of the damage regions (c_i), and the horizontal and vertical locations of the centers of the damage regions ($\epsilon_i^x, \epsilon_i^y$) and the corresponding values estimated by the inverse characterization process with the Optimal NDT design (Optimal), the Single-Objective NDT design (Single-Obj.), and the Control NDT design (Control) and the resulting relative L_2-Error and the relative L_∞-Error of the Young's modulus distributions as well as the mean and standard deviation over all five trials for Example 2 - Plate with two damage locations.

Trial		D_1	c_1	ϵ_1^x	ϵ_1^y	D_2	c_2	ϵ_2^x	ϵ_2^y	L_2-Error	L_∞-Error
1	Target	0.300	0.006	0.200	0.300	0.800	0.009	0.800	0.400	-	-
	Optimal	0.170	0.016	0.290	0.940	0.932	0.007	0.808	0.388	0.044	0.181
	Single-Obj.	0.290	0.027	0.098	0.669	0.506	0.018	0.888	0.272	0.120	0.469
	Control	0.987	0.013	0.306	0.821	0.822	0.008	0.794	0.386	0.149	0.987
2	Target	0.700	0.005	0.400	0.800	0.500	0.002	0.700	0.700	-	-
	Optimal	0.657	0.005	0.391	0.866	0.401	0.005	0.714	0.706	0.054	0.446
	Single-Obj.	0.691	0.024	0.031	0.615	0.565	0.012	0.923	0.836	0.149	0.691
	Control	0.173	0.011	0.039	0.593	0.706	0.002	0.651	0.500	0.080	0.706
3	Target	0.500	0.006	0.100	0.700	0.900	0.009	0.800	0.200	-	-
	Optimal	0.498	0.008	0.252	0.628	0.700	0.012	0.925	0.148	0.131	0.616
	Single-Obj.	0.748	0.008	0.216	0.645	0.662	0.013	0.927	0.148	0.137	0.720
	Control	0.840	0.019	0.154	0.559	0.798	0.014	0.807	0.056	0.181	0.831
4	Target	0.700	0.008	0.800	0.200	0.900	0.006	0.600	0.700	-	-
	Optimal	0.108	0.021	0.864	0.240	0.406	0.015	0.641	0.687	0.085	0.191
	Single-Obj.	0.843	0.021	0.715	0.385	0.288	0.030	0.584	0.712	0.174	0.844
	Control	0.544	0.015	0.779	0.260	0.260	0.023	0.537	0.584	0.097	0.324
5	Target	0.800	0.007	0.200	0.200	0.600	0.004	0.200	0.800	-	-
	Optimal	0.087	0.023	0.143	0.232	0.761	0.004	0.074	0.500	0.107	0.764
	Single-Obj.	0.308	0.014	0.271	0.033	0.999	0.021	0.066	0.626	0.188	0.999
	Control	0.636	0.030	0.164	0.057	0.401	0.010	0.175	0.863	0.114	0.614
Optimal									Mean	0.084	0.440
									Std. Dev.	0.036	0.257
Single-Obj.									Mean	0.154	0.744
									Std. Dev.	0.028	0.196
Control									Mean	0.124	0.692
									Std. Dev.	0.041	0.249

1.6   CONCLUSIONS

A method for optimal NDT design for applications in material characterization and damage identification of solid continua was presented. The proposed method extends the concept of maximizing response sensitivity for optimal NDT design in a generally applicable way for NDE/material characterization problems, and in particular, includes an additional objective to prevent redundancy of the test information. Through simulated examples of frequency response function-based NDT, the optimal NDT design method was shown to yield NDT specifications with substantially higher measurement sensitivity and lower measurement re-dundancy than alternate (more traditional) NDT designs. Moreover, the improved NDT design features were shown to provide consistently more accurate material characterization results than the alternate testing techniques, indicating the ability of the optimized NDT design to produce a substantially more solvable inverse problem. Overall, this work provides a generalized foundation for deterministic optimal NDT design, but it should be noted that accounting for the omnipresence of uncertainty (e.g., system defects) is of critical importance to moving forward in this field and the field of inverse problems as a whole. As such, future efforts are expected to focus on extending such NDT design approaches to simultaneously provide robustness in the presence of uncertain features of the systems considered.

2.0 A COMPUTATIONAL APPROACH FOR ROBUST NONDESTRUCTIVE TEST DESIGN MAXIMIZING CHARACTERIZATION CAPABILITIES FOR SOLIDS AND STRUCTURES SUBJECT TO UNCERTAINTY

2.1 ABSTRACT

A robust approach to nondestructive test (NDT) design for material characterization and damage identification in solids and structures is presented and numerically evaluated. The generally applicable approach combines maximization of test sensitivity with minimization of test information redundancy, while simultaneously minimizing the effects of uncertain system parameters to determine optimal NDT parameters for robust nondestructive evaluation. In addition, to maintain reasonable computational expense while also allowing for general applicability, a stochastic collocation technique is presented for the quantification of uncertainty in the robust design metrics. The robust NDT design approach was tested through simulated case studies based on the characterization of localized variations in Young's modulus distributions in aluminum structural components utilizing steady-state dynamic surface excitation and localized measurements of displacement and compared to a purely deterministic NDT design approach. The robust design approach is shown to produce substantially different NDT designs than the analogous deterministic strategy. More importantly, the robust NDT designs are shown to provide significant improvements in the ability to accurately nondestructively evaluate structural properties for the cases considered when there is significant uncertainty in system parameters and/or aspects of the NDT implementation.

2.2 INTRODUCTION

An extensive amount of work has been focused in recent years on developing methods for the solution of a wide variety of inverse problems in applied mechanics and engineering, including characterization, design, and/or control of complex systems [85, 4, 6, 8, 10, 62, 83]. Of particular interest to the present work are inverse problems relating to the use of nondestructive testing (NDT) to evaluate various properties of different in-service structures/systems, such as aircraft [55], spacecraft [69], and bridges [80], which can be an important step in predicting the health of these systems, to improve safety and operational efficiency. Although various research efforts, particularly the computational approaches, directed towards the solution of these types of inverse characterization problems have made significant strides, there are still several common challenges, most often relating to the ill-posedness of the inverse problems in the form of nonexistent or non-unique solutions along with the excessive computational expense associated with many solution algorithms. These inverse problem challenges are even more highlighted when considering the various omnipresent sources of noise in the NDT measurements and uncertainty in the features of the systems to be characterized. One effective approach to overcome, or at least relieve some of the ill-posedness of nondestructive evaluation (NDE) inverse problems is to address the complementary inverse problem of robust optimal design of the NDT itself. NDT design can also be an important step for the feasibility of implementing a particular NDT system by optimizing the amount of resources needed to characterize the system (e.g., minimizing the number of sensors), subject to monetary cost, time, and/or accessibility constraints. Moreover, in order to design a NDT that is truly optimal in practice, the NDT design must consider the uncertainties in all system parameters that have an effect on the system response, even those that may not be the chosen variable of interest of the associated characterization problem.

In recent years, several different approaches have been developed for NDT design, most often specifically optimizing the placement of sensors, for structural health monitoring and NDE [11, 38, 87, 47, 65, 64, 66, 77]. Naturally, one of the most important features of NDT design methods is the metric used to define the quality of a given design (e.g., sensor distribution). The existing methods are diverse in the definition of this design metric and

have shown mixed results, including those relying on *ad hoc* approaches such as maximizing the contribution of the sensor locations to the mode shapes of the structure [38], as well as statistical or probabilistic approaches, such as those that minimize the information entropy of the system that corresponds to the uncertainty of the model parameters [64], and more theory-driven techniques, such as those that attempt to maximize the probability of detection for the system [11, 32]. The methods to then employ these metrics to improve NDT quality are also varied, with some taking a system identification approach that iteratively discard or include candidate sensors to optimally represent the target metrics [74, 43, 44], while others use more traditional optimization strategies, creating an objective function directly relating to the NDT quality metric of choice and applying iterative optimization to minimize or maximize the objective function [68, 91]. Overall, the majority of existing NDT optimization methods are specialized with respect to the intended quantity to be evaluated and the nature of the NDT apparatus in which they can be used, and most approaches are limited to consideration of the number of sensors and their corresponding locations, with little attention paid to actuation location, orientation, excitation frequency/duration, and redundancy of the measured information. Alternatively, a potentially generalizable approach was presented in [67] that relies on maximizing the sensitivity of the nondestructively generated frequency responses with respect to the damage parameters to be determined, while simultaneously minimizing the number of sensors employed. Notghi and Brigham [60] then extended this concept of maximizing response sensitivity for optimal NDT design in a generally applicable way for NDE and material characterization problems, while also including an additional NDT design objective to prevent redundancy of the testing information and further ensure the efficient use of NDT resources.

Significantly fewer NDT design efforts have attempted to address robustness with respect to uncertainty in the variables outside of the set of variables to be evaluated by the NDE. Examples include the work by Castro-Triguero et al. [23] which used the highest optimal selected sensors from samples generated by Monte Carlo simulation in stochastic space as well work by Azarbayejani et al.[11], which rely on the highest probability of detection. Additionally, one substantial challenge/limitation to address additional uncertain parameters in the NDT design is the added computational expense of propagating the uncertainty and

quantifying the effect of these uncertain parameters on the NDT and ultimately the resulting NDE. Most of the existing NDT design methods incorporating uncertainty have used the traditional computationally expensive Monte-Carlo techniques, which when combined with the expense of the numerical analysis (e.g., finite element analysis) that is often used to predict system responses, can lead to these approaches becoming computationally prohibitive for many practical problems with any degree of complexity. Another critical aspect which effect the performance of NDT design is to address the uncertainty that exists in these NDT systems [41, 74] .

The current work presents a generalized approach for optimal design of NDT that is robust to system uncertainty, discussed within the context of material characterization problems in solid continua. In particular, the approach extends the concept of maximizing test response sensitivity and minimizing measurement redundancy to include the maximization of robustness to uncertainty of system parameters that are not part of the set to be inversely characterized with the NDT. In addition, the techniques presented address the issues of computational expense of uncertainty quantification by incorporating Smolyak method, which significantly reduces the number of numerical analyses of the system response necessary to quantify the effects of system uncertainty in comparison to the standard Monte-Carlo techniques, while maintaining ease of implementation. In the following section a general inverse characterization solution framework for the NDE problems to be considered for context is outlined. Then, the approach for robust optimal NDT design to maximize inverse characterization solution capabilities is presented. Lastly, simulated examples relating to characterization of semi-localized variations in the Young's modulus distribution in structures from frequency-response-based NDT are presented, including simulated experiments to show inverse characterization capabilities, which is followed by the concluding remarks.

2.3 INVERSE PROBLEM FORMULATION AND SOLUTION STRATEGY

The present work utilized a standard generally-applicable optimization-based computational approach for inverse material characterization to motivate the NDT design approach and the method to test the efficacy of potential NDT designs. As is typical, this computational inverse mechanics approach for material characterization consists of first constructing a numerical representation (e.g., finite element model) of the behavior of the target system that is parameterized with respect to the unknown system properties and subject to whatever particular NDT that has been chosen to be applied. Then, an objective functional is constructed that quantifies the difference between the measured response from the NDT and that predicted by the numerical representation for any given admissible set of system properties. An example objective functional for the inverse problem of determining the spatial distribution of some material property over the system domain could be written as

$$J(E(\vec{x})) = \left\| \frac{R^{ndt}(\vec{\gamma}_k) - R^{sim}(\vec{\gamma}_k, E(\vec{x}))}{R^{ndt}(\vec{\gamma}_k)} \right\|_k , \tag{2.1}$$

where $E(\vec{x})$ is the material property (e.g., Young' modulus) distribution to be determined, $\vec{x} \in \Omega$ is the spatial position vector in the domain of the system Ω, R^{ndt} is the measured response of the system from the NDT, R^{sim} is the simulated estimate of the system response from the NDT for a given material property estimate, $\{\vec{\gamma}_k\}_{k=1}^{N_T}$ is the set of all NDT combinations (e.g., excitation frequency, sensor location, actuator location, etc.), with a total number of NDT measurement combinations of N_T (assuming for the presentation here that the NDT produces a set of discrete measurements), and $\|.\|_k$ is some suitable metric norm that combines the contributions of each measurement to produce the total error functional J. Lastly, all that is necessary is to minimize the objective functional $(J(E(\vec{x})))$ with respect to the material properties $(E(\vec{x}))$ to produce an estimate to the inverse problem solution. There are generally two classes of optimization techniques that are used to solve these typically non-convex optimization problems, those that are gradient-based [59, 54], which iteratively update solution estimates based upon the gradient of the objective functional with respect to the parameters to be determined and are relatively computationally efficient, but local in nature (i.e., may often stall in the search process at a local minimum of the objective

functional, and those that are non-gradient-based [21, 37, 76], which commonly (although not always) include some stochastic component within the search process to provide global search capabilities, but have relatively higher computational expense.

Regardless of the specifics of this form of inverse solution process (e.g., specific numerical representation, objective functional form, and/or optimization algorithm), of paramount importance is that the error functional, which is obtained from the measured response of the system for the chosen NDT, is sensitive to changes in the material properties to be determined. The measurement sensitivity clearly has a direct effect on the capability of gradient-based methods to traverse the search space of the problem, but even for non-gradient-based methods there is a universal need to have an objective functional that varies significantly with respect to the unknown properties throughout the search space to provide sufficient information to direct the search process towards a solution. At the same time, the error functional should be insensitive (i.e., robust) to parameters that may have some degree of uncertainty, but are not considered as part of the set of properties to be determined through the inverse solution process (e.g., potential errors in the estimation of the actuation location and/or the support conditions of a structure, etc.). These uncertainties could be viewed as leading to a loss of accuracy in the computational representation of the system response, and if the system response were to be significantly sensitive to these uncertain parameters, an inverse solution may be unattainable, or worse yet, any apparent solution may be dramatically incorrect.

2.4 ROBUST OPTIMAL NONDESTRUCTIVE TEST DESIGN

The first hypothesis enforced here is that to maximize the capability of a NDE process to inversely characterize material properties, the associated NDT (potentially including consideration of sensor and actuator locations, orientations, and frequencies, along with any other conceivable aspect) should somehow maximize the sensitivity of the response measurements with respect to changes in the unknown properties. Thus, the problem of designing the optimal NDT can firstly be cast as an optimization problem to maximize a functional that

quantifies the change in the measured response with respect to the unknown properties to be determined of the following form,

$$P\left(\{\vec{\gamma}_k\}_{k=1}^{N_T}\right) = \left\|D_E R^{sim}(\vec{\gamma}_k, E(\vec{x}))\right\|_{\Omega,k}, \qquad (2.2)$$

where $D_E R^{sim}$ is some form of the derivative or gradient of the response functional with respect to the material properties and $\|.\|$ is now some suitable metric norm that combines the sensitivity contributions of each measurement with respect to the material properties over the entire domain of the system (Ω) to produce the total sensitivity functional P. However, as was shown in [61], only considering 2.2 may lead to a poor use of NDT resources by resulting in redundant measurement information (e.g., sensors nearly overlapping), particularly for cases in which candidate locations of sensors and actuator are continuously (or nearly continuously) distributed throughout the domain of the system. As such, a second functional can be formed that quantifies the similarity of the response measurements in terms of orthogonality (i.e., responses are less similar if they are closer to orthogonal) as

$$\theta_{i,j} = \arccos\left(\frac{\langle R^{sim}(\vec{\gamma}_i, E(\vec{x})), R^{sim}(\vec{\gamma}_j, E(\vec{x}))\rangle}{\|R^{sim}(\vec{\gamma}_i, E(\vec{x}))\| \, \|R^{sim}(\vec{\gamma}_j, E(\vec{x}))\|}\right), \quad \forall \, i,j \in [1, N_T], \, i \neq j, \qquad (2.3)$$

where $\langle .,.\rangle$ is a suitable inner product operator (e.g., standard vector dot product if the responses are simply a discrete vector of sensor measurements) and $\|.\|$ can be defined such that

$$\left\|R^{sim}(\vec{\gamma}_i, E(\vec{x}))\right\|^2 = \langle R^{sim}(\vec{\gamma}_i, E(\vec{x})), R^{sim}(\vec{\gamma}_i, E(\vec{x}))\rangle. \qquad (2.4)$$

Simultaneously maximizing 2.2 and 2.3 can thus provide an estimate to the optimal NDT with respect to maximum response sensitivity and minimum measurement redundancy.

While the above two functionals allow for the design of a sensitive test with respect to the desired properties with non-redundant testing information (i.e., efficiently utilizing system resources), neither addresses the potential uncertainty that could exist within system parameters that are not part of the desired NDE properties (i.e., properties that may not be known exactly, but will not be a solution variable of the NDE). As discussed previously, if the system response is sufficiently sensitive to these uncertain system parameters, then the inverse solution capabilities may suffer greatly, and the optimality would be lost for an NDT design constructed based upon only 2.2 and 2.3. Alternatively, a more robust approach that

takes into account sources of uncertainty within the system could be constructed along the lines of the following general form for a robust optimization problem,

$$\text{Optimize} \left\{ \mu_{\vec{\varphi}} \left[\vec{f^d}(\vec{d}, \vec{\varphi}) \right], \nu_{\vec{\varphi}} \left[\vec{f^u}(\vec{d}, \vec{\varphi}) \right] \right\}, \tag{2.5}$$

where $\vec{d}$ is the set of deterministic system parameters (i.e., those deemed to have negligible uncertainty and/or effect on the system response, which can be represented by their nominal values), $\vec{\varphi}$ is the set of uncertain system parameters, $\vec{f^d}$ is the vector of representations of performance or cost objective functionals, $\vec{f^u}$ is the vector of dispersion measures relating to the objective functionals with respect to the uncertain parameters, $\mu_{\vec{\varphi}}$ is the expected value operator with respect to the uncertain parameters, and $\nu_{\vec{\varphi}}$ is the dispersion measure operator (e.g., variance or standard deviation). For an optimal NDT design the performance functionals can be simply defined with respect to the sensitivity and redundancy objectives defined above. Then, to ensure robustness of the NDT design, the second core hypothesis for the present study is that the effects of the uncertain parameters on the NDE process can be minimized by minimizing the variance of the system response measured by the NDT with respect to the uncertain parameters. Combining these three concepts (i.e., maximum sensitivity, minimum redundancy, and maximum robustness), the robust optimal NDT design problem can be cast as a multi-objective optimization problem as

$$\underset{\{\vec{\gamma}_k\}_{k=1}^{N_T}}{\text{Maximize}} \begin{cases} \left\| \mu_{\vec{\varphi}} \left[D_E R^{sim}(\vec{\gamma}_k, E(\vec{x}), \vec{\varphi}) \right] \right\|_{\Omega,k} \\[2mm] \underset{\substack{i,j \in [1,N_T] \\ i \neq j}}{\text{Minimum}} \quad \arccos \left(\frac{\left\langle \mu_{\vec{\varphi}} \left[R^{sim}(\vec{\gamma}_i, E(\vec{x}), \vec{\varphi}) \right], \ \mu_{\vec{\varphi}} \left[R^{sim}(\vec{\gamma}_j, E(\vec{x}), \vec{\varphi}) \right] \right\rangle}{\left\| \mu_{\vec{\varphi}} [R^{sim}(\vec{\gamma}_i, E(\vec{x}), \vec{\varphi})] \right\| \left\| \mu_{\vec{\varphi}} [R^{sim}(\vec{\gamma}_j, E(\vec{x}), \vec{\varphi})] \right\|} \right) \\[2mm] \frac{1}{\left\| Var_{\vec{\varphi}} [R^{sim}(\vec{\gamma}_k, E(\vec{x}), \vec{\varphi})] \right\|_{\Omega,k}} \end{cases}, \tag{2.6}$$

where $Var_{\vec{\varphi}}$ is the variance operator with respect to the uncertain parameters.

In order to solve the optimization problem in 2.6 it is necessary for the properties that will ultimately be determined by the NDE $(E(\vec{x}))$ to be initialized. Fortunately, for many NDE problems (e.g., damage characterization) some nominal values are available based upon assumed initial (i.e., healthy) properties of the system, are these property values can often be a natural selection for the initialization of the NDT design problem. More importantly, the calculation of the moments (i.e., expected values and variance) for the components of

the multi-objective optimization problem typically requires the solution of stochastic partial differential equations (SPDE) and boundary conditions (i.e., a boundary value problem that represents the physical behavior of the system subject to the specific NDT that is dependent upon the uncertain parameters). The solution of a SPDE and boundary conditions is a nontrivial task, and depending upon implementation, can require considerable computational expense. As such, it is important to choose a generally applicable approach that maintains reasonable computational expense, and the particular solution approach utilized herein is described in detail in the following.

2.4.1 Stochastic Collocation for SPDE Solution Approximation

Consider the following general form of a SPDE representing the behavior of the system of interest subject to nondestructive testing,

$$\mathcal{L}(\vec{x}, t, \vec{d}, \vec{\varphi}; R(\vec{x}, t, \vec{d}, \vec{\varphi})) = f(\vec{x}, t, \vec{d}, \vec{\varphi}), \tag{2.7}$$

where R is the total system response field, $\mathcal{L}$ is a differential operator, and f is some source term. Based upon the SPDE, the objective is to somehow determine the desired moments of the system response field with respect to the uncertain parameters. There exist a variety of different numerical methods that can be used for the solution of an SPDE with boundary conditions, including both intrusive and non-intrusive approaches, with each having varying benefits and shortcomings [12, 14, 36, 33, 88]. For simplicity within this proof-of-concept study of an approach to address system uncertainty within NDT design a non-intrusive stochastic collocation method was implemented, which is generally applicable, relatively simple to implement, and reasonably computationally efficient.

Stochastic collocation methods are based on the use of interpolation functions in combination with collocation points samples from the stochastic space to approximate the distribution of the response in the stochastic space, which can then be used to approximate the moments of the desired components with minimal computational expense [88, 13, 58]. For brevity in the following formulation it is assumed that each uncertain parameter can be mapped to a domain of $[-1, 1]$ and all previously given deterministic dependencies of the

responses field are implied, while the dependency on the deterministic parameters will be explicitly stated. Thus, for any single dimension (i.e., component) of the stochastic space the stochastic collocation approximation of the response field can be written as

$$\overline{R}(\varphi) = U^m(R) = \sum_{j=1}^{m} R(\varphi_j) \cdot L_j(\varphi) \, , \tag{2.8}$$

where L_j are the standard Lagrange interpolating polynomials and m is the number of collocation points in the stochastic space.

For the multivariate case (e.g., n-dimensional) the one-dimensional approximation can be simply applied in each of the multiple dimensions to produce the full tensor product formula [15]

$$\left(U^{i_1} \otimes \cdots \otimes U^{i_n} \right)(R) = \sum_{j_1=1}^{m_1} \cdots \sum_{j_n=1}^{m_n} R(\varphi_{j_1}^{i_1}, ..., \varphi_{j_n}^{i_n}) \cdot \left(L_{j_1}^{i_1} \otimes \cdots \otimes L_{j_n}^{i_n} \right) \, . \tag{2.9}$$

Direct application of this tensor product formula requires what can be an excessive number of collocation points $(m_1 \times \cdots \times m_n)$ with increasing stochastic space dimension. Therefore, the sparse grid approaches seek to substantially reduce the total number of required collocation points without significantly diminishing the approximation accuracy. For the present study sparse grids were constructed using the Smolyak algorithm, in which the sparse interpolant is given as [86, 15]

$$A_{q,n} = \sum_{q-n+1 \leq |\vec{i}| \leq q} (-1)^{q-|\vec{i}|} \cdot \binom{n-1}{q-|\vec{i}|} \cdot (U^{i_1} \otimes \cdots \otimes U^{i_d}), \tag{2.10}$$

where n is the number of stochastic dimensions, $q - n$ is the order of interpolation, $\vec{i} = (i_1, ..., i_n)$ and $|\vec{i}| = i_1 + \cdots + i_n$ (note that i_k conceptually represents the level of interpolation along the the kth direction). To compute $A_{q,n}(R)$ the response function should be evaluated at the sparse grid points given by

$$\mathcal{H}_{q,n} = \bigcup_{q-n+1 \leq |i| \leq q} (\Theta^{i_1} \otimes \cdots \otimes \Theta^{i_n}), \tag{2.11}$$

where $\Theta^{i_k} = (\varphi_1^{i_k}, ..., \varphi_{m_k}^{i_k})$. Lastly, for the present work the extrema of the Chebyshev polynomials were chosen to be used as the foundation for the interpolation. As such, the collocation points for any $m_i > 1$ were defined as

$$\varphi_j^i = -cos\frac{\pi.(j-1)}{m_i - 1}, \text{ for } j = 1, \cdots, m_i, \tag{2.12}$$

and $\varphi_1^i = 0$ if $m_i = 1$.

2.5   EXAMPLES AND DISCUSSION

In order to show the potential capabilities of the presented approach for creating a robust optimal NDT design, two simulated case studies were considered regarding characterization of material stiffness distributions, specifically semi-localized reductions in stiffness within aluminum structures as could potentially be used to represent and characterize states of damage. To perform the assessment NDT designs were created based on the robust approach shown, and for comparison purposes NDT designs were also created through a purely deterministic approach only maximizing the sensitivity and minimizing the redundancy metrics (utilizing Equations. 2.2 and 2.3 as shown in [61]). In order to calculate the NDT design metrics the baseline (i.e., undamaged) material parameters were assumed to be defined by a homogeneous Young's modulus of $E_H = 69\ GPa$ and a Poison's ratio of $\nu = 0.3$.

Several inverse characterization cases were examined applying the respective NDT designs to produce measurement data with which to estimate simulated material distributions and assess the effectiveness of the NDT design approaches. Specifically, for each case study the inverse characterization processes were repeated for four different damage scenarios, and to test the robustness of the designs for each scenario 10 different randomly generated sets of the uncertain system parameters were applied to generate the NDT, while the mean values of the parameters were used for the inverse solution process (i.e., 40 total inverse characterization trials for each case). An important note is that one of the key steps in the analysis of any stochastic system is the identification and parameterization of the significant uncertain properties of the system with a finite number of independent random variables with

appropriate distributions, which requires some amount of expert knowledge and intuition [89]. For simplicity in the present work all chosen uncertain parameters were assumed to have uniform distributions, but it should be noted that the approach discussed is generally applicable regardless of the specific distributions assumed.

2.5.1 Nondestructive Testing and Forward Problem

As discussed, the concepts presented are intended to be generally applicable, however, for context the examples considered herein consisted of structures tested with frequency-response-based NDT. For both case studies the NDT consisted of a localized harmonic actuation applied normal to the surface of the structure over a range of frequencies and the resulting steady-state harmonic vertical displacement amplitude was measured at a set of discrete sensor locations for each actuation frequency. Frequency-response-based NDT was chosen for its implementation simplicity and proven diagnostic capability, and although displacement measurement is not particularly common, approaches have been developed to acquire such measurements [78, 75]. Therefore, the potential NDT design parameters for the test cases were the set of sensor locations, $\left\{ \vec{X}_{Sk} \right\}_{k=1}^{N_s}$ (however, it should again be noted that the approach presented could easily be applied to any number of NDT parameters, not just sensor locations).

All simulations were performed using the finite element method, including the simulations to design the NDT, to simulate the measurement data, and to solve the inverse problems. The structures were assumed to behave linearly elastically with respect to the NDT described, and therefore, defined by steady-state dynamic solid mechanics. In addition, the actuation was assumed to be reasonably represented by an applied harmonic pressure force to the surface of the structure being analyzed. Therefore, the SPDE and boundary conditions governing the behavior of the structures and used to predict the moments of the displacement NDT measurement responses with respect to the uncertain parameters ($\vec{\varphi}$) can be written as

$$\nabla \cdot \sigma(\vec{x}, \omega, \vec{\varphi}) + \omega^2 \rho(\vec{x}, \vec{\varphi}) \vec{u}(\vec{x}, \omega, \vec{\varphi}) = \vec{0}, \quad \forall \, \vec{x} \in \Omega,$$

$$\sigma(\vec{x}, \omega, \vec{\varphi}) \cdot \vec{n}(\vec{x}) = \vec{T}(\vec{x}, \omega, \vec{\varphi}), \quad \forall \, \vec{x} \in \Gamma_T, \tag{2.13}$$

$$\vec{u}(\vec{x}, \omega, \vec{\varphi}) = \vec{u}^0(\vec{x}, \omega, \vec{\varphi}), \quad \forall \, \vec{x} \in \Gamma_u,$$

where σ is the stress tensor, ω is the excitation frequency, ρ is the density, $\vec{u}$ is the displacement vector, $\vec{n}$ is the unit normal to the surface, $\vec{T}$ is the applied traction vector, $\vec{u}^0$ is the vector of applied displacement boundary conditions, Ω is the domain of the structure, Γ_T is the portion of the domain boundary with applied traction boundary conditions, and Γ_u is the portion of the domain boundary with applied displacement boundary conditions. In particular, for the examples considered herein the input uncertainties were assumed to only exist within the parameters of the essential boundary conditions ($\vec{u}^0$), the natural boundary conditions ($\vec{T}$), and the density (ρ). The Smolyak algorithm discussed in the previous section was applied to approximate the moments of the displacement response.

The NDT design metrics were discretized and approximated as shown in [61]. In addition, the solutions to the multi-objective optimization problems for both the robust designs and the deterministic comparison designs can be described by sets of non-dominated solutions with respect to the various objectives (i.e., Pareto fronts). For the examples herein the one solution for the NDT designs were selected using the 'nearest to ideal point' method, which selects the point that has the minimum euclidean distance to an imaginary 'ideal point' that has the optimal value for each objective function separately [46, 45]. Lastly, to add realism to the simulated examples and to partially relieve the inverse crime inherent in simulated experiments, in addition to randomly generating values of the uncertain parameters for the simulated NDT, 1% Gaussian white noise was added to all responses for each simulated NDT case prior to applying the inverse characterization procedure as

$$R^{ndt} = R_0^{ndt}(1 + 0.01\aleph), \tag{2.14}$$

where R_0^{ndt} is the original simulated test response without noise and $\aleph$ is a normally distributed random variable with zero mean and unit variance.

2.5.2 Inverse Characterization Problem

To test each NDT design measurement data was generated as described above with various randomly generated Young's modulus distributions, and the computational inverse solution approach discussed in Section 2.3 was applied to estimate the Young's modulus distributions as if they were unknown. In particular, for all examples cases the Young's modulus distribution was assumed to vary due to semi-localized changes defined by a radial basis function (RBF) representation as

$$E(\vec{x}) = \left[1 - D \cdot \exp\left(-\frac{\|\vec{x} - \vec{\epsilon}\|^2}{c} \right) \right] \times 69 \; GPa, \tag{2.15}$$

where $\|.\|$ represents the standard l_2-norm, and the material parameters to be determined by the inverse characterization process were the Young's modulus percent reduction corresponding to each RBF, D, the center of the RBF, $\vec{\epsilon}$, and the breadth of the RBF, c. For the characterization solution process for all tests the material parameters were assumed to be bounded as follows: $D \in [0,1]$, $\vec{\epsilon} \in [0,1] \times [0,1]$, and $c \in [0, 0.1]$.

Again, note that as would be often done in practice a single value of the uncertain parameters (the mean value here) was used for all inverse solution analyses, whereas randomly generated values of those parameters were used to simulate the NDT measurements (i.e., the input parameters for the analyses used to generate the NDT measurements were not identical to those for the inverse solution process). Therefore, the objective functional employed for the inverse solution process to measure the difference between the "experimental" measurements and those predicted by the optimization simulations was defined as

$$J\left(E(\vec{x})\right) = \frac{1}{N_w N_S} \sum_{k=1}^{N_w} \sum_{i=1}^{N_S} \left| \frac{R^{ndt}(\omega_k, \vec{X}_{Si}, \vec{X}_F, \vec{\varphi}^r) - R^{sim}(\omega_k, \vec{X}_{Si}, \vec{X}_F, \vec{\bar{\varphi}}, E(\vec{x}))}{R^{ndt}(\omega_k, \vec{X}_{Si}, \vec{X}_F, \vec{\varphi}^r)} \right|, \tag{2.16}$$

where $\vec{\varphi}^r$ is a randomly generated set of the uncertain parameters and $\vec{\bar{\varphi}}$ is the set of mean values of the uncertain parameters. Lastly, the surrogate-model accelerated random search

(SMARS) optimization algorithm [18] was applied to identify the Young's modulus distribution that minimizes 2.16, and therefore, estimate the solution to the inverse characterization problem. The SMARS algorithm iteratively combines the global random search algorithm with a locally applied surrogate model method, and provides an optimization technique that maintains global search capabilities over relatively large parameter domains while having a relatively low computational expense.

2.5.3 Example 1 - Plate

The first inverse material characterization case study consisted of a $1m \times 1m$ aluminum plate, shown schematically in Figure 2.1, with a precisely known density value of $\rho = 2700kg/m^3$ (i.e., uncertainty in this material property was assumed to be negligible), but with uncertainty in the boundary condition. The first uncertain boundary condition consisted of a fixed region of uncertain length along the bottom, for which the start of the fixity was assumed to begin at the bottom left corner of the plate and terminate at a horizontal length described by a uniformly distributed random variable $X_{BC} \sim U(0.62, 0.76)m$, with the remaining boundary assumed to be free to displace. In addition, the simulated NDT consisted of applying a $1kPa$ harmonic load to a $5cm$ region normal to the top surface of the plate, and the horizontal position of the load was assumed to be described by a uniformly distributed random variable $X_F \sim U(0.66, 0.74)m$. For simplicity of the design problem and based on preliminary analysis, four vertical displacement sensors were determined to be sufficient. Additionally, to avoid placing a sensor too near to a support condition or the actuation force the potential sensor locations were restricted to $\vec{X}_{Si} \in [0, 1] \times [0.02, 0.98]m$. The excitation frequencies of the NDT were also assumed to be predetermined as 6 evenly spaced values from $100Hz$ to $1000Hz$. Therefore, the unknown NDT parameters to be determined consisted of the locations of each of the four sensors. To quantify the uncertainty for the robust NDT design (i.e., to calculate the metrics in 2.6) for this case study a 2 dimensional level 7 Smolyak method was used, which required 705 realization (i.e., 705 finite element analyses of the system).
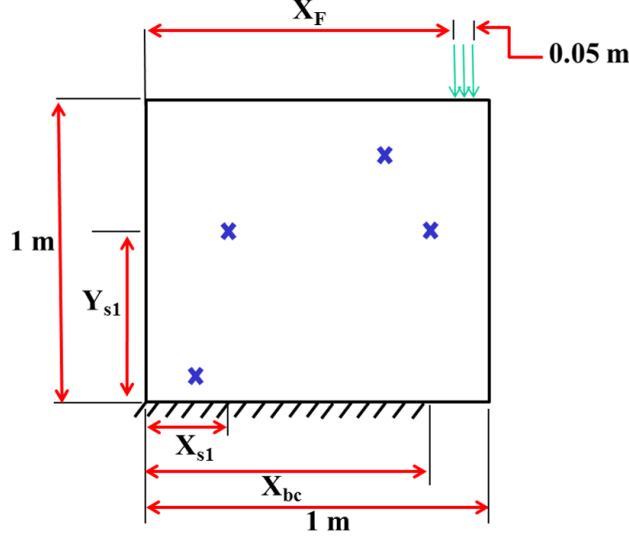
Figure 2.1: Schematic for Example 1, displaying the sensor locations, (X_{Si}, Y_{Si}), the length of the essential boundary condition, X_{bc}, and the actuator location, X_F.

Utilizing the robust optimal NDT design process presented the locations of the sensors were determined to be (shown in Fig. 2.2(a)): $\vec{X}_{S1} = (0.7, 0.85)m$, $\vec{X}_{S2} = (0.8, 0.6)m$, $\vec{X}_{S3} = (0.35, 0.6)m$, and $\vec{X}_{S4} = (0.2, 0.1)m$. Alternatively, for the deterministic comparison case (using the deterministic NDT design approach approach shown in [60]) the sensor locations were determined to be (shown in Fig. 2.2(b)): $\vec{X}_{S1} = (1.0, 0.7)m$, $\vec{X}_{S2} = (0.8, 0.7)m$, $\vec{X}_{S3} = (0.5, 0.9)m$, and $\vec{X}_{S4} = (0.7, 0.3)m$. Note that for the deterministic NDT design the mean values of the uncertain parameters (i.e., $X_{BC} = 0.69m$ and $X_F = 0.70m$) were used. Since neither the support condition nor the actuation location were centered on the plate it is not surprising that neither optimal design is symmetric (note that this was done intentionally to avoid a trivial or non-unique result for this test case). What is more interesting, however, is that the two sensor distributions were significantly different, with only one sensor from each of the two groups that could be considered particularly close to one another. This substantial difference in the sensor layouts at least initially indicates the significance of addressing robustness to uncertainty within the NDT design process. Furthermore, Table 2.1 shows that the robust NDT design has significantly lower values for the sensitivity and
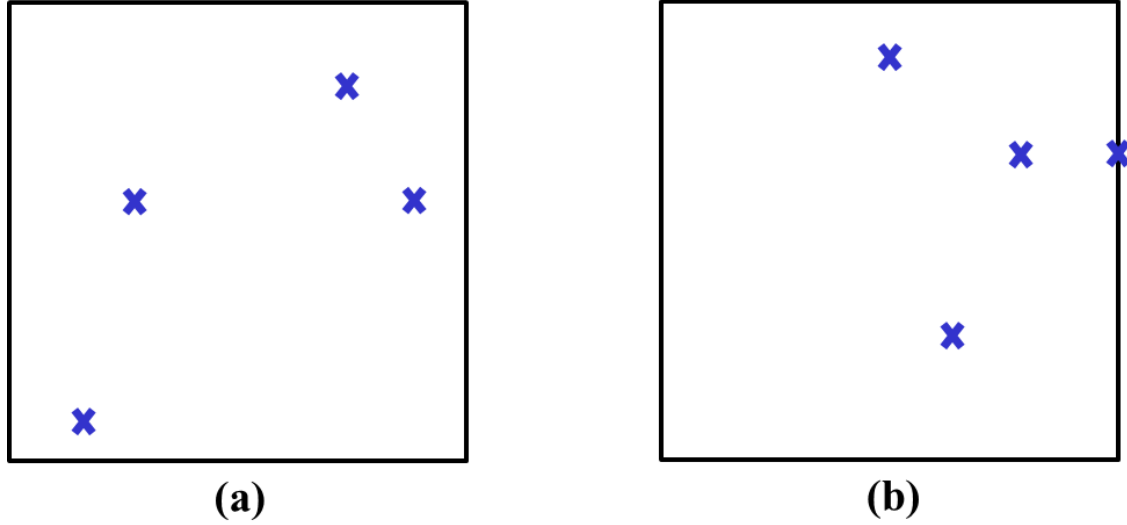
Figure 2.2: Schematics of the NDT designs for Example 1, including the sensor locations determined for (a) the robust NDT design and (b) the deterministic NDT design.

redundancy metrics when calculated based on the mean values of the uncertain parameters compared to the deterministic NDT design, which is not necessarily surprising, but indicates the significance of the robustness as a competing objective.

As discussed, in order to test the true effectiveness of each NDT design, the inverse characterization process was applied for four different material distribution (i.e., damage) scenarios, shown in Figure 2.3, with the measurement data from each NDT design utilized in turn. Again, note that to test the robustness and solution consistency the inverse process was repeated 10 times for each damage scenario, each time with a different randomly generated value of the uncertain parameters, while the forward modeling used in the inverse solution process assumed the uncertain parameters maintained the mean value. The stopping criteria for the SMARS optimization process to estimate the material parameters for the inverse characterization for this example was set as a maximum of 5700 finite element analyses for all trials.

Table 2.1: Values of the sensitivity metric 2.2 and the redundancy metric (the minimum value of 2.3) based on the mean values of the uncertain parameters ($X_{BC} = 0.69m$ and $X_F = 0.70m$) for the robust NDT design and the deterministic NDT design for Example 1.

NDT Design Case	Sensitivity Metric	Redundancy Metric
Robust	2.43×10^4	$81°$
Deterministic	3.54×10^4	$89°$
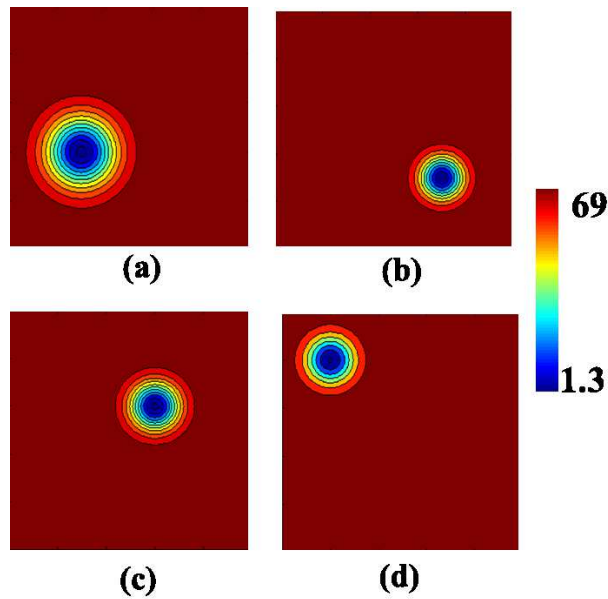
Figure 2.3: Four (a-d) randomly generated target (i.e., simulated experimental) spatial distributions of the Young's modulus for testing the inverse characterization capabilities of each NDT design for Example 1 (color contours are in units of GPa).

Table 2.2 shows the RBF parameters for each damage scenario used to simulate the sensor measurement data for both the robust and the deterministic NDT designs, the respective means and standard deviations of the inversely estimated RBF parameters from the 10 trials of each scenario with each NDT, as well as the corresponding mean and standard deviation of the relative L_2-Error and the relative L_∞-Error for the resulting Young's modulus distributions with respect to the distributions used to generate the sensor measurement data.

On average over all inverse characterization tests for the four damage scenarios there was a reduction in the relative L_2-Error of approximately 3% for the robust NDT design compared to the deterministic design, with specific trials ranging between a 1% and 5% reduction. However, what may be more significant, especially for problems searching for localized or semi-localized property variations such as this (noting that the L_2-Error averages over the domain), is that the average relative L_∞-Error for the results of the robust NDT design was less than half of that for the deterministic NDT design for each damage scenario considered. Furthermore, one specific observation from the inverse characterization results was that the robust NDT design tended to underestimate the magnitude of the damage (i.e., change in stiffness), but the robust design provided a significantly more accurate estimate of the location of the damage region in comparison to the deterministic NDT design. As was not unexpected, there were several tests within the set of 40 in which the deterministic NDT design produced slightly more accurate results than the robust NDT design. Upon close inspection it was found that the tests in which the deterministic NDT design was more accurate typically had values of the randomly generated uncertain system parameters relatively near to the mean values that were used in the inverse solution process. Thus, since the deterministic NDT achieves a higher sensitivity for the measurement quantities assuming no error in the assumed system parameters, the exected result of a more accurate characterization occurs for those cases where that error is relatively small. Alternatively, when the error in the uncertain parameters of the system is not negligible for the inverse solution process (as would often be the case in reality) the robustness of the NDT design becomes essential, and the robust NDT design approach consistently improves the solution capabilities.

Table 2.2: Target values for the unknown damage parameters $D_1 c_1)$ and $\epsilon_1^x, \epsilon_1^y$, the mean and standard deviation of the unknown values as estimated by the inverse characterization process for all 10 trials with both the robust NDT design and the deterministic NDT design, and the corresponding mean and standard deviation of the relative L_2 and relative L_∞.

		D_1	c_1	ϵ_1^x	ϵ_1^y	L_2-Error	L_∞-Error
	Target Value	0.8	0.02	0.3	0.4	-	
	Robust NDT Design						
	Mean	0.44	0.026	0.36	0.25	0.13	0.30
	Std. Dev.	0.31	0.007	0.06	0.13	0.03	0.22
Damage 1	Deterministic NDT Design						
	Mean	0.79	0.018	0.33	0.29	0.15	0.65
	Std. Dev.	0.03	0.005	0.11	0.16	0.03	0.12
	Target Value	0.7	0.008	0.7	0.3	-	
	Robust NDT Design						
	Mean	0.38	0.022	0.60	0.28	0.09	0.35
	Std. Dev.	0.20	0.006	0.11	0.08	0.02	0.20
Damage 2	Deterministic NDT Design						
	Mean	0.70	0.020	0.57	0.40	0.12	0.68
	Std. Dev.	0.09	0.008	0.24	0.24	0.02	0.09
	Target Value	0.8	0.01	0.6	0.6	-	
	Robust NDT Design						
	Mean	0.41	0.028	0.61	0.50	0.10	0.33
	Std. Dev.	0.30	0.003	0.13	0.01	0.03	0.28
Damage 3	Deterministic NDT Design						
	Mean	0.76	0.014	0.70	0.73	0.11	0.65
	Std. Dev.	0.06	0.007	0.16	0.14	0.03	0.18
	Target Value	0.5	0.01	0.2	0.8	-	
	Robust NDT Design						
	Mean	0.15	0.014	0.26	0.70	0.06	0.09
	Std. Dev.	0.16	0.009	0.15	0.11	0.01	0.09
Damage 4	Deterministic NDT Design						
	Mean	0.49	0.025	0.45	0.63	0.11	0.48
	Std. Dev.	0.12	0.008	0.12	0.03	0.02	0.11
	Robust NDT Design					Mean	0.10	0.27
						Std. dev.	0.03	0.12
Total	Deterministic NDT Design					Mean	0.13	0.62
						Std. dev	0.02	0.09

2.5.4 Example 2 - Airfoil

Finally, to examine the capabilities of the NDT design approaches for a more realistic scenario, the second simulated case study consisted of analysis of an aluminum airfoil structure based upon the standard NACA-0012 cross section, shown schematically in Figure 2.4.

Again, the NDE objective was to determine a semi-localized change in the Young's modulus distribution throughout the airfoil as could be representative of a damage scenario. However, to simplify the inverse problem slightly, the semi-localized change in the Young's modulus distribution was assumed to be known to only occur in the upper portion of the airfoil and the value was kept constant through the thickness of the airfoil. Therefore, the two-dimensional parameterization of the Young's modulus described by 2.15 was still applicable as the description of the in plane Young's modulus distribution of the top half of the airfoil. Similarly to the previous example, the airfoil was assumed to be partially fixed on one side with the remaining boundaries free to displace, but with uncertain parameters in this case describing the length of the upper and lower portions of the boundary separately (as shown in Figure 2.4(b)). The length of the supported regions on the upper and lower boundaries were assumed to be described respectively by uniformly distributed random variables $X_{UBC} \sim U(0.66, 0.74)m$ and $X_{LBC} \sim U(0.62, 0.76)m$. In addition, for this examples case, the homogeneous material density of the airfoil was also assumed to be an uncertain parameter described by a uniformly distributed random variable $\rho_a \sim U(2565, 2835)kg/m^3$. The simulated NDT consisted of applying a $1kPa$ harmonic load to a circular region normal to the top surface of the airfoil with a radius of $0.09m$ and centered at $(X_f, Y_f) = (0.41, 0.8)m$, while the displacement amplitude was measured at four sensors that were restricted to the top surface of the upper portion of the airfoil. As before, the excitation frequencies of the NDT were assumed to be predetermined as 3 evenly spaced values from $100Hz$ to $300Hz$, and the unknown NDT parameters to be determined consisted of the sensor locations. Again, to avoid the boundary the potential sensor locations were restricted to $\vec{X}_{Si} \in [0, 1.0] \times [0.02, 1.0]m$. To quantify the uncertainty for the robust NDT design for this case study a 3 dimensional level 7 Smolyak method was used, which required 2561 realization of the system.
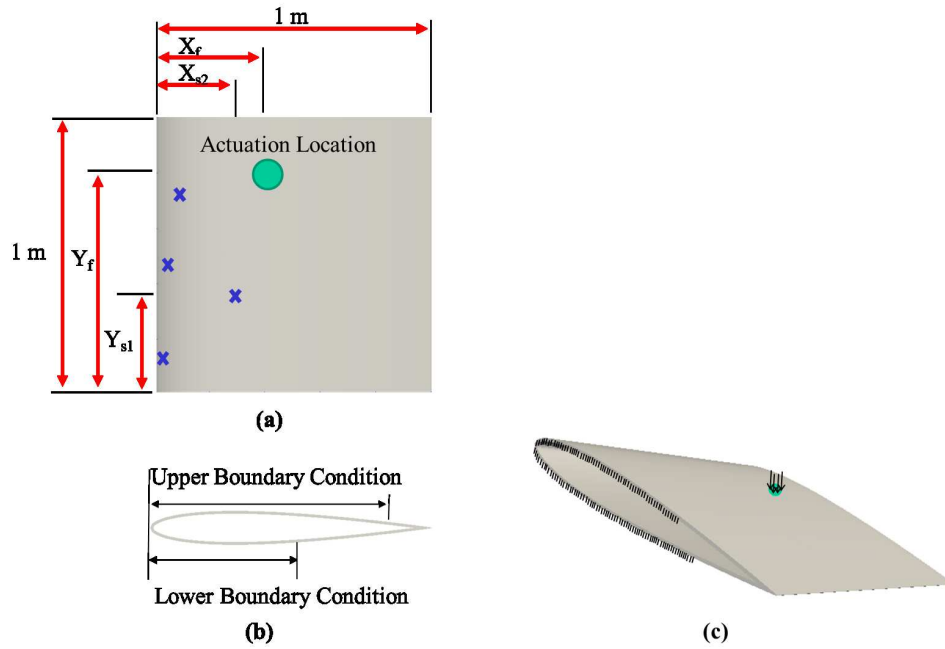
Figure 2.4: Schematic for Example 2, including (a) the top view of the airfoil, displaying the sensor locations, (X_{Si}, Y_{Si}), the location of the actuation (X_f, Y_f), (b) the cross section of the airfoil, displaying the upper and lower boundary conditions, and (c) The 3D view of the airfoil.
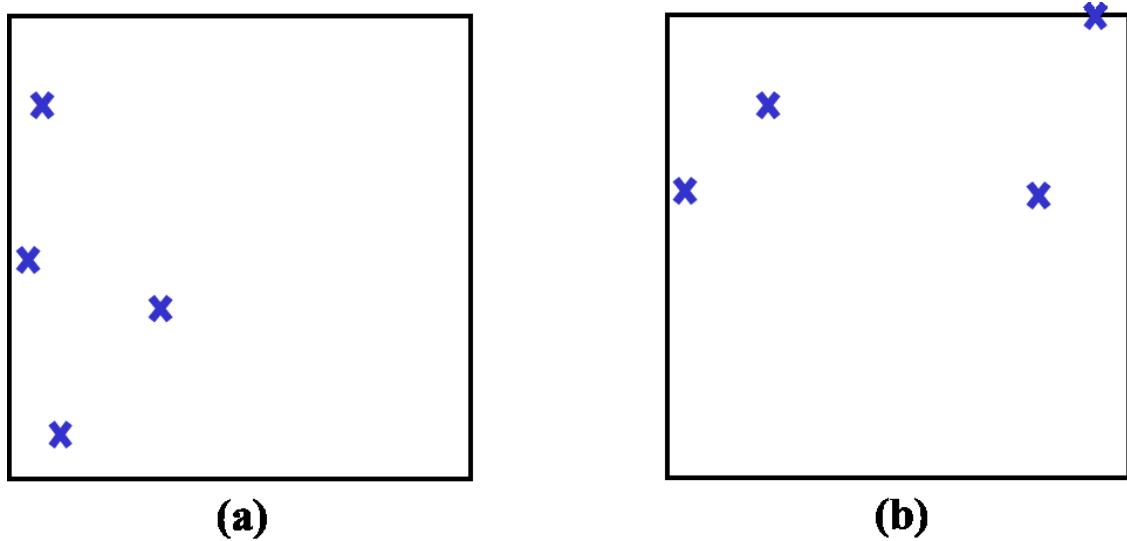
Figure 2.5: Top view schematics of the NDT designs for Example 2, including the sensor locations determined for (a) the robust NDT design and (b) the deterministic NDT design.

For this airfoil case the sensor locations for the robust NDT design were determined to be (shown in Fig. 2.5 (a)): $\vec{X}_{S1} = (0.31, 0.40)m$, $\vec{X}_{S2} = (0.043, 0.50)m$, $\vec{X}_{S3} = (0.076, 0.70)m$, and $\vec{X}_{S4} = (0.005, 0.10)m$. Again, to provide a deterministic (i.e., non-robust) comparison, the sensor locations for the deterministic NDT design were determined to be (shown in Fig. 2.5 (b)): $\vec{X}_{S1} = (0.005, 0.60)m$, $\vec{X}_{S2} = (0.25, 0.80)m$, $\vec{X}_{S3} = (0.80, 0.60)m$, and $\vec{X}_{S4} = (0.924, 1.0)m$. Similarly to the first example, the mean values of the uncertain parameters were used for the deterministic NDT design (i.e., $X_{UBC} = 0.70m$, $X_{LBC} = 0.69m$, and $\rho_a = 2700kg/m^3$), and as before, the sensor distributions identified for the robust design and the deterministic design were considerably different. The effectiveness of each NDT design was once again tested by applying the inverse characterization process for four different damage scenarios shown in Fig. 2.6.

The stopping criteria for the SMARS optimization process to estimate the material parameters for the inverse characterization for this example was set as a maximum of 17500 finite element analyses for all trials. Table 2.3 shows the RBF parameters for each damage scenario used to simulate the sensor measurement data for both the robust and the
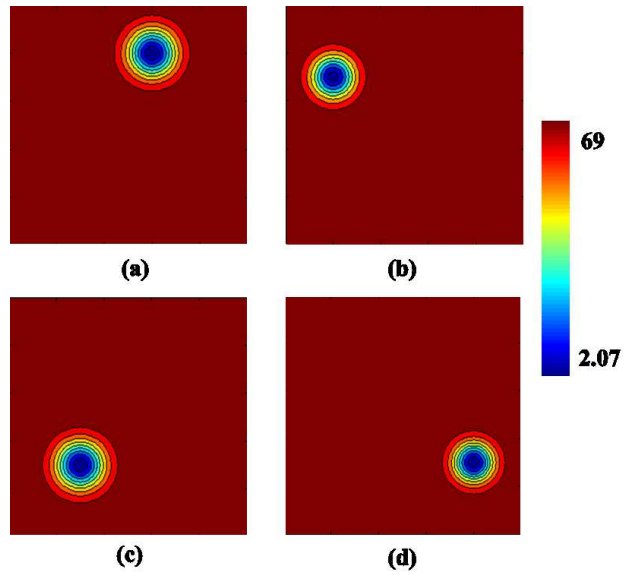
Figure 2.6: Top view of the four (a-d) randomly generated target (i.e., simulated experimental) spatial distributions of the Young's modulus for testing the inverse characterization capabilities of each NDT design for Example 2 (color contours are in units of GPa).

deterministic NDT designs, the respective means and standard deviations of the inversely estimated RBF parameters from the 10 trials of each scenario with each NDT, as well as the corresponding mean and standard deviation of the relative L_2-Error and the relative L_∞-Error for the resulting Young's modulus distributions with respect to the distributions used to generate the sensor measurement data.

The results for the characterization tests, particularly the relative errors comparing the robust design to the deterministic design, were surprisingly highly consistent for this significantly more complex test case compared to the first example. On average, the robust NDT design produced inverse material characterization results that were significantly more accurate than the deterministic NDT design, particularly in terms of the L_∞-Error in the Young's modulus, and the capabilities of the robust NDT design were especially highlighted for the individual trials where the variation in the uncertain parameters was significant.

2.6 CONCLUSIONS

A generalized approach for robust NDT design for applications in material characterization and damage identification of solids and structures was presented. The approach extends the concept of deterministic NDT design for maximum test response sensitivity and minimum measurement redundancy to include the maximization of robustness to uncertainty of system parameters that are not included in the set to be inversely characterized with the NDT. In addition, the Smolyak stochastic collocation method was presented as a means to efficiently calculate the response moments with respect to the uncertain parameters of the system utilized in the robust NDT design metrics in a way that is generally applicable. Through simulated examples of frequency response function-based NDT, the robust NDT design approach was shown to provide considerably different optimal NDT parameters in comparison to an analogous deterministic NDT design method. Moreover, example cases of applying the respective optimal NDT designs showed that the robust NDT design consistently produced more accurate material characterization results for the NDE of structural components in which system uncertainty exists in comparison to the deterministic NDT design.

57

Table 2.3: Target values for the unknown damage parameters D_1, c_1, and $\epsilon_1^x, \epsilon_1^y$, the mean and standard deviation of the unknown values as estimated by the inverse characterization process for all 10 trials with both the robust NDT design and the deterministic NDT design, and the corresponding mean and standard deviation of the relative L_2 and relative L_∞.

		D_1	c_1	ϵ_1^x	ϵ_1^y	L_2-Error	L_∞-Error
	Target Value	0.7	0.01	0.6	0.8	-	
	Robust NDT Design						
	Mean	0.76	0.003	0.84	0.91	0.09	0.74
Damage 1	Std. Dev.	0.20	0.001	0.18	0.13	0.01	0.21
	Deterministic NDT Design						
	Mean	0.89	0.008	0.85	0.92	0.12	0.88
	Std. Dev.	0.23	0.005	0.19	0.14	0.02	0.23
	Target Value	0.6	0.008	0.2	0.7	-	
	Robust NDT Design						
	Mean	0.94	0.020	0.22	0.60	0.12	0.74
Damage 2	Std. Dev.	0.11	0.008	0.02	0.08	0.05	0.18
	Deterministic NDT Design						
	Mean	0.96	0.019	0.13	0.59	0.14	0.94
	Std. Dev.	0.04	0.005	0.15	0.04	0.01	0.04
	Target Value	0.7	0.01	0.3	0.3	-	
	Robust NDT Design						
	Mean	0.74	0.022	0.17	0.42	0.13	0.71
Damage 3	Std. Dev.	0.13	0.008	0.07	0.04	0.02	0.11
	Deterministic NDT Design						
	Mean	0.89	0.019	0.07	0.46	0.15	0.87
	Std. Dev.	0.08	0.008	0.13	0.07	0.03	0.11
	Target Value	0.7	0.007	0.8	0.3	-	
	Robust NDT Design						
	Mean	0.27	0.002	0.94	0.15	0.07	0.24
Damage 4	Std. Dev.	0.23	0.001	0.08	0.19	0.01	0.22
	Deterministic NDT Design						
	Mean	0.54	0.006	0.87	0.09	0.09	0.54
	Std. Dev.	0.30	0.005	0.20	0.15	0.03	0.30
	Robust NDT Design				Mean	0.10	0.61
					Std. dev.	0.03	0.24
Total	Deterministic NDT Design				Mean	0.12	0.81
					Std. dev	0.03	0.18

3.0   ADAPTIVE REDUCED-BASIS GENERATION FOR REDUCED-ORDER MODELING IN SPARSE GRID APPROXIMATIONS OF STOCHASTIC PARTIAL DIFFERENTIAL EQUATIONS

3.1   ABSTRACT

A generally applicable algorithm for creating a computationally efficient approximation of a system response that is defined by a boundary value problem is presented. More specifically, the approach presented is focused on substantially reducing the computational expense required to approximate the solution of a stochastic partial differential equation, particularly for the purpose of estimating the solution to an associated inverse problem. In order to achieve this computational efficiency, the approach combines reduced-basis reduced-order modeling with a sparse grid collocation surrogate modeling technique to estimate the response of the system of interest with respect to any designated unknown parameters, including those that may be considered to have significant uncertainty and/or those that are entirely unknown and sought to be determined through an inverse solution procedure. The reduced-order modeling component includes a novel generally applicable algorithm for adaptive generation of a data ensemble based on a nested grid technique, to then create the reduced-order basis. The capabilities and potential applicability of the approach presented are displayed through two simulated case studies regarding inverse characterization of material properties for two different physical systems/processes involving some amount of significant uncertainty. The first case study considered characterization of an unknown localized reduction in stiffness of a structure from simulated frequency response function based nondestructive testing. Then, the second case study considered characterization of an unknown temperature-dependent thermal conductivity of a solid from simulated thermal

testing. Overall, the surrogate modeling approach was shown through both simulated examples to provide accurate solution estimates to inverse problems for systems represented by stochastic partial differential equations with a fraction of the typical computational cost.

3.2 INTRODUCTION

There are a large number of important inverse problems in engineering mechanics, covering applications from characterization to design of complex physical systems, and a corresponding large amount of work involving the solution of these problems. [85, 4, 6, 8, 10, 62, 83]. One effective approach for solving such inverse problems in mechanics has been to use a numerical analysis tool, such as finite element analysis, to predict the forward response of the system under consideration and then combine nonlinear optimization to find the unknown properties to "best match" the response of the numerical model with the desired or measured response of the system [2, 84, 51, 83, 60]. Although various research efforts, have been directed towards such computational methods for the solution of inverse problems and have made significant strides, there are still several common challenges, most often relating to the ill-posedness of the inverse problems in the form of nonexistent or non-unique solutions along with the excessive computational expense associated with many solution algorithms. In particular, regardless of the solution approach (e.g., gradient based [59, 54] or non-gradient-based optimization [21, 37, 76], etc.), solving an inverse problem using a computational solution procedure commonly requires a relatively large number of evaluations of the forward response of the system. Moreover, the computational expense drastically increases if considering uncertainty within the system, since the forward problem then involves a stochastic partial differential equation (SPDE) (which is considerably expensive on its own).

There are several different approaches that have been developed for the solution of SPDEs [36, 12, 88]. Whether the approach to address the uncertainty is intrusive (i.e., modifies the deterministic boundary value problem) or non-intrusive (i.e., only uses results from the deterministic boundary value problem), these solution approaches typically require a sub-

stantial amount of computational expense. As such, there has been considerable effort to attempt to reduce the computational expense of SPDE solutions, both for intrusive [17] and non-intrusive approaches [42]. Sparse grid approximation approaches are one particular computationally efficient solution technique that builds a low-cost approximation (i.e., surrogate model) of the SPDE and has shown considerable promise for being used in approximating SPDE solutions [79, 88]. The sparse grid methods are non-intrusive, and therefore, easy to implement, requiring only the solution of uncoupled deterministic problems, and use substantially fewer evaluations of the boundary value problem in comparison to the traditional Monte Carlo non-intrusive methods, without sacrificing accuracy [12]. However, even with the reduction in the number of boundary value problem evaluations required, constructing a sufficiently accurate sparse grid approximation of the SPDE for high-dimensional or highly nonlinear problems (among other complexities) that can provide accurate approximations for the entire parameter space can still require a substantial number of analyses of the associated deterministic boundary value problem, even to the point of being computationally prohibitive in some cases [52]. To address this challenge, one potential approach could be to use a two step process to reduce the overall computational expense to a feasible level, first reducing the cost of the deterministic boundary value problem with a reduced-basis reduced-order modeling technique, that can then be used with a sparse grid approach to construct the surrogate model for the SPDE solution approximation.

Reduced-basis-type model reduction approaches that identify the relatively low-dimensional basis that is optimal in some sense for representing the physics of the system of interest have been used to produce efficient and accurate numerical representations for several different applications in mechanics [40, 25, 63, 20]. By not replacing the boundary value problem governing the mechanics of interest as would be done with surrogate modeling approaches, reduced-basis ROM techniques are more computationally expensive than surrogate modeling approaches, but are typically capable of more accurate approximations, particularly for extrapolating throughout the space of potential system inputs. This ROM approach has also been recently extended to stochastic problems with the work by Boyaval et al. [17] that created reduced-basis ROMs to estimate the solution of an SPDE. There are different strategies to determine the low-dimensional basis, but the focus of the work herein is on

methods that derive the "optimal" basis from a given set of potential fields for the system of interest. These given fields can be either experimentally measured or numerically simulated with different values of the system input parameters, depending on capabilities. There are also different approaches to process these given fields to produce a basis. For example, proper orthogonal decomposition (POD) has been used in several studies [9, 49, 1] to extract the basis from a given dataset that is optimal in the average L_2-error sense for representing the given fields. Alternatively, other works, including the work by Boyaval et al. relating to SPDEs, have simply used Gram Schmidt orthogonalization to directly convert the given fields into an orthogonal basis [17]. Yet, a more important question that is not often addressed in ROM studies is how to generate (e.g., select the system inputs to numerically simulate with full-order analysis) the initial set of potential fields used to create the basis. The majority of the previous work has used some form of fixed sampling, often simply uniformly sampling the input parameter space [53]. Alternatively, one approach that has been developed and referred to as "certified reduced basis methods" uses *a posteriori* error estimation to iteratively add to a set of potential fields to minimize the error of the resulting ROM with respect to the estimated error bound [72]. However, the ability to generate and ensure accuracy of the *a posteriori* error estimate for the ROM with a given PDE can be nontrivial and a potentially costly task. A different approach was presented by Brigham and Aquino [20] to generate the dataset for ROM creation that was based on creating the set of potential fields that were maximally diverse in a sense within the solution space. However, this maximum diversity approach was only applicable as presented for problems relating to solid mechanics of rate-dependent materials. Overall, no clear approach exists as of yet that is generally applicable, easy to implement, and computationally inexpensive to generate a suitable dataset and ultimately an accurate ROM.

The current work presents an approach to substantially reduce the computational expense required to approximate the solution of a stochastic PDE, particularly for the purpose of estimating the solution to an associated inverse problem. In order to achieve this computational efficiency, the approach presented combines reduced-basis reduced-order modeling with a sparse grid collocation surrogate modeling technique to estimate the response of the system of interest with respect to both the inverse problem unknowns and the uncertain

system parameters. In the following section a general inverse problem solution framework is outlined. Then, the approach for using the sparse grid method as a system response surrogate model is presented, which is followed by an adaptive method for generating efficient and accurate reduced-order models for the solution of SPDEs. Lastly, the capability of this computationally efficient approach to provide accurate solution estimates to inverse problems of systems represented by SPDEs with a fraction of the typical computational cost is shown through simulated examples involving both solid mechanics and heat transfer.

3.3 METHODS

For context, the methods are presented with respect to inverse characterization problems based upon some type of physical system measurements (e.g., displacements or temperatures) given the associated boundary conditions and some knowledge of significant epistemic uncertainty in certain system parameters. Furthermore, the present work utilizes a standard generally-applicable optimization-based computational approach for inverse problem solution approximation to evaluate the ROM strategy. As is typical, the computational inverse mechanics approach consists of first constructing a numerical representation of the behavior of the target system that is parameterized with respect to the unknown system properties. Then, an objective functional is constructed that quantifies the difference between the measured response and the response predicted by the numerical representation for any given admissible set of system properties. Lastly, all that is necessary is to minimize the objective functional with respect to the unknown system properties to produce an estimate to the inverse problem solution. As an example, a common objective functional for the inverse solution approach could have the following form:

$$J(\vec{h}) = \frac{\left\| R^{mes} - R(\vec{c}, \vec{h}) \right\|}{\| R^{mes} \|},$$
(3.1)

where $\vec{h}$ is the vector of unknown parameters (e.g. parameters defining a material property distribution) to be determined through the inverse solution process, R^{mes} is the measured

response of the system, R is the simulated estimate to the system's response for a given parameter set estimate, $\vec{c}$ is the vector of uncertain system parameters, and $\|.\|$ is some suitable metric norm that combines the contributions of all measurement information to produce the total scalar error functional.

A critical point is that the calculation of the simulated response of the structure with respect to different parameter estimates using traditional analysis methods (e.g., finite element analysis) can be computationally expense for many realistic applications, which can lead to the inverse solution process becoming computationally infeasible (especially when addressing uncertainty). Therefore, rather than using computationally expensive methods to numerically simulate the system response estimate, the present work instead utilizes a substantially more computationally inexpensive surrogate modeling strategy to produce a tool to simulate the system response (R) with negligible computational expense. In particular, this work presents a combined ROM-collocation strategy to effectively and efficiently generate a surrogate model of the system response with respect to both the inverse problem unknowns and the uncertain system parameters. As outlined in the following, this approach not only uses a collocation method to obtain the surrogate model for the system response, but generates and uses a ROM to create this surrogate model with a substantial savings in computational expense in comparison to traditional techniques at each step in the process and for the overall solution procedure.

3.3.1 Sparse Grid Collocation Method for Forward Model Approximation

A sparse grid collocation method was selected to create the system response surrogate model for the present work due to its capabilities to provide accurate approximations of smooth functions in high dimensions based on a relatively small number of function evaluations, as has been shown in several works relating to global optimization [73, 31]. For the purposes of the sparse grid collocation method, the vector of unknown/inverse problem parameters ($\vec{h}$) and the vector of uncertain system parameters ($\vec{c}$) are treated equivalently, and therefore, are combined into a single parameter vector, $\vec{\varphi} = [\vec{h}, \vec{c}]^T$, for this presentation.

The basic collocation approach uses Lagrange interpolating polynomials and the tensor product technique to incorporate all dimensions of the parameter space to define the surrogate model approximation of the system response in terms of a higher-order (e.g., finite element analysis) model of the system response evaluated at each collocation point in the parameter space as:

$$\left(U^{i_1} \otimes \cdots \otimes U^{i_n}\right)(R^{HO}) = \sum_{j_1=1}^{m_1} \cdots \sum_{j_n=1}^{m_n} R^{HO}(\varphi_{j_1}^{i_1}, ..., \varphi_{j_n}^{i_n}) \cdot \left(L_{j_1}^{i_1} \otimes \cdots \otimes L_{j_n}^{i_n}\right) , \qquad (3.2)$$

where R^{HO} is the higher-order model response, L_j^i is the jth standard Lagrange interpolating polynomial corresponding to the ith parameter and m_i is the number of collocation points for the ith parameter. Note that each parameter is typically mapped to a domain of $[-1, 1]$ for this implementation. While this collocation approach is a relatively straightforward technique overall, the selection of the collocation points is a nontrivial task. With the total number of evaluations of the higher-order model of the system response being equivalent to $m_1 \times \cdots \times m_n$, the creation of the surrogate model by simply using uniformly spaced collocation points in the parameter space can be excessively computationally expensive, even for a relatively inexpensive higher-order model (R^{HO}). Thus, the sparse grid approach is used here to reduce the computational cost by significantly reducing the total number of required collocation points without significantly sacrificing accuracy of the surrogate model.

For the present study, the Smolyak algorithm [86, 15] was used for the sparse grid construction. At its core, the Smolyak algorithm creates a sparse grid interpolant to be utilized in place of the tensor product above as:

$$A_{q,n} = \sum_{q-n+1\leq|\vec{i}|\leq q} (-1)^{q-|\vec{i}|} \cdot \binom{n-1}{q-|\vec{i}|} \cdot (U^{i_1} \otimes \cdots \otimes U^{i_d}), \qquad (3.3)$$

where n is the total number of system parameters (i.e., dimension of $\vec{\varphi}$), $q - n$ is the order of interpolation, $\vec{i} = (i_1, ..., i_n)$, and $|\vec{i}| = i_1 + \cdots + i_n$ (note that i_k conceptually represents the level of interpolation along the the kth direction). To compute the surrogate model response approximation, $R = A_{q,n}(R^{HO})$, the response function should be evaluated at the sparse grid points given by

$$\mathscr{H}_{q,n} = \bigcup_{q-n+1\leq|i|\leq q} (\Theta^{i_1} \otimes \cdots \otimes \Theta^{i_n}), \qquad (3.4)$$

65

where $\Theta^{i_k} = (\varphi_1^{i_k}, ..., \varphi_{m_k}^{i_k})$. Lastly, there are different potential choices for the nested grid to define the collocation points in the parameter space, such as the Gauss Patterson approach [22] or the Clenshaw-Curtis approach [82].

Utilizing a sparse grid approximation allows for construction of the surrogate model with orders of magnitude reduction in the number of higher-order analyses required compared to a standard tensor product implementation with approximately the same level of accuracy. However, sparse grids are still affected by the "curse of dimensionality," and the number of analyses required for relatively high-dimensional parameter spaces can become excessive if the higher-order model being approximated requires a substantial computational expense (as would often be the case if using traditional finite element analysis to produce the system response here). Thus, the present works adds one more layer of computational savings by building and using a ROM (instead of a commonly used full-order finite element analysis) for the higher-order analysis in the surrogate model creation, as detailed in the following.

3.3.2 Adaptive Nested Sampling for Reduced-Order Model Generation

The reduced-order modeling strategy utilized herein is the reduced-basis approach, which in essence, identifies the low-dimensional basis that is optimal in some sense to replace the standard higher-order generalized (e.g., polynomial) bases typically used within a numerical PDE solution strategy (e.g., weak form Galerkin finite element method)[70]. This approach was chosen since it balances the improvement in computational expense with the capability to maintain accurate generalization over the parameter space that is afforded by maintaining the physics of the problem through the PDE, which is still included in the solution procedure, in contrast to alternate ROM techniques. The following discussion of an approach to create such an accurate physics-based ROM is presented in a general format, which can be used for a variety of mechanics, including both steady-state and transient processes, etc., and could even be applicable as a direct replacement in a computational inverse problem solution procedure (although, that was not the focus of the work herein).

To understand the ROM approach, first consider the following general form of a SPDE representing the behavior of a system of interest (arbitrarily shown as transient and with only essential boundary conditions for clarity, but could equivalently be utilized for a static problem, a problem in the frequency domain, and/or a problem with other boundary conditions as well):

$$\frac{\partial^n \vec{u}(\vec{x}, t; \vec{\varphi})}{\partial t^n} = F(\vec{\varphi}; \vec{u}(\vec{x}, t; \vec{\varphi})), \quad \forall \, \vec{x} \in \Omega$$

$$\frac{\partial^r \vec{u}(\vec{x}, t = 0; \vec{\varphi})}{\partial t^r} = g_r(\vec{x}; \vec{\varphi}), \quad \forall \, \vec{x} \in \Omega, \; \text{for} \; r = 0, ..., n - 1 \tag{3.5}$$

$$\vec{u}(\vec{x}, t; \vec{\varphi}) = \vec{u}^0(\vec{x}, t; \vec{\varphi}) \; \forall \, \vec{x} \in \Gamma,$$

where $\vec{u}$ is the primary system response field (e.g., displacement in solid mechanics), $\vec{x}$ is the spatial position, t is time, F is a spatial differential operator, n is the number of temporal derivatives, g_r are the known initial conditions, $\vec{u}^0$ is the known boundary condition, Ω is the spatial domain, and Γ is the domain boundary. The core hypothesis of the reduced-basis reduced-order modeling approach considered in the present work is that a relatively small number of full-order (i.e., traditional finite element) analyses based upon different values of the input parameters of interest ($\vec{\varphi}$) contain fundamental information about the spatial distribution of potential solution fields of the boundary value problem (BVP) and can be used to derive a low-dimensional basis that can predict the solution fields for a range of input parameters (not just the specific parameter values used to generate the set of full-order analyses) with reasonable accuracy.

The proper orthogonal decomposition (POD) method was used herein to derive the basis to be used from a set of previously generated full-order analysis solution fields [19]. As detailed in Appendix A, POD creates the basis that is optimal in an L_2 average sense for approximating the given solution fields. Assuming such a m-dimensional basis has been created, the solution of the SPDE (Equation 3.5) can be approximated by a linear combination of the basis functions (i.e., modes) as:

$$\vec{u}(\vec{x}, t; \vec{\varphi}) = \sum_{i=1}^{m} a_i(t; \vec{\varphi}) \vec{\phi}_i(\vec{x}) \tag{3.6}$$

where $a_i(t; \vec{\varphi})$ is the ith modal coefficient to be determined by the numerical analysis to approximate the solution of the system given a new set of system input parameters, whether

those parameters are unknowns to be determined through an inverse solution process or other uncertain parameters of the system. Applying the Galerkin projection procedure, the solution approximation (Equation 3.6) can be substituted into the governing SPDE (Equation 3.5) to obtain the weak form of the SPDE that can be used to approximate the modal coefficients as:

$$\frac{\partial^n \alpha_c(t; \vec{\varphi})}{\partial t^n} = \left(F\left(\vec{\varphi}; \sum_{i=1}^{N} \alpha_i(t; \vec{\varphi}) \vec{\phi}_i(\vec{x}) \right), \vec{\phi}_c(\vec{x}) \right)_{L_2}, \quad \text{for } c = 1, ..., m, \tag{3.7}$$

with the initial conditions given as:

$$\alpha_c(t = 0; \vec{\varphi}) = (g_r(\vec{x}; \vec{\varphi}), \phi_c)_{L_2}, \quad \text{for } r = 0, ..., n - 1, \quad c = 1, .., m, \tag{3.8}$$

where $(\cdot, \cdot)_{L_2}$ is the standard L_2 inner product. Note that for the case of fixed essential boundary conditions, the modes will automatically satisfy the essential boundary conditions for the system of interest.

Of paramount importance is that a critical question still remains unanswered from the above formulation, which is how to select the set of input parameters used to create the set of full-order analyses that will be utilized to then create the POD basis and ultimately the ROM. In particular, to see a true benefit from this ROM strategy, this dataset must be generated in such a way to limit the number of full-order simulations necessary to ensure sufficiently accurate generalization of the ROM over the admissible range of the input parameters of interest. As such, the following presents an adaptive strategy to incrementally select the parameter set values to be used to create full-order analysis fields (referred to as "snapshots" from here on) and build the ROM to minimize a measure of the potential ROM solution error.

3.3.2.1 Adaptive Nested Grid Snapshot Generation: The core of this incremental snapshot generation approach is the use of a nested grid strategy to select the associated parameter set values along with a local refinement procedure to select additional parameter set values adaptively in the region of the parameter space with the highest approximation error. In addition, the parameter space sampling that is used to create the ROM can be done in such a way (as was done herein) that a portion of the parameter space grid points corresponding to the snapshots are the exact same points as a portion of the collocation points that will then be used to create the surrogate model (as described in Section 3.3.1). Since, the points in the parameter space corresponding to the full-order analyses are naturally the most accurate (in the ROM context), having the grids overlap in this two stage (i.e., ROM to surrogate model) process will ensure that the information with the highest possible accuracy is used to create the numerical representation of the system response that will ultimately be used in the inverse problem solution procedure.

The algorithm developed for adaptive nested grid snapshot generation is outlined in Algorithm 1. For the present work, an *ad hoc* approach was used to estimate the approximation

---

Algorithm 1 - Adaptive Nested Grid Snapshot Generation

1: Randomly generate a ROM test set of parameter sets and corresponding response fields with full-order simulation.
2: Generate an initial set of snapshots from the parameter sets that are defined based on the chosen nested grid type and initial level (L).
3: Create a reduced-basis ROM from the set of snapshots.
4: Evaluate the ROM for each parameter set in the ROM test set and calculate the average relative L_2-error with respect to the full-order simulations ($E_{L_2}^{ave}(ROM)$).
5: **while** $\left(E_{L_2}^{ave}(ROM) > E_{Level}^{tol}\right)$ **do**
6:      Increase the grid level: $L = L + 1$, and generate the additional associated snapshots.
7:      Create a reduced-basis ROM from the set of snapshots.
8:      Evaluate the ROM for each parameter set in the ROM test set and calculate $E_{L_2}^{ave}(ROM)$.
9: **end while**
10: Calculate the maximum relative L_∞-error with respect to the full-order simulations ($E_{L_\infty}^{max}(ROM)$).
11: **while** $\left(E_{L_\infty}^{max}(ROM) > E_{Local}^{tol}\right)$ **do**
12:      Identify the parameter set ($\vec{S}$) corresponding to $E_{L_\infty}^{max}(ROM)$.
13:      Generate additional snapshots from parameter sets based on a hypercube of length l centered at $\vec{S}$ in the parameter space.
14:      Create a reduced-basis ROM from the set of snapshots.
15:      Evaluate the ROM for each parameter set in the ROM test set and calculate $E_{L_\infty}^{max}(ROM)$.
16: **end while**

---

error of the ROM based on a randomly generated set of full-order analysis response fields (i.e., "ROM test" set) to drive the adaptive snapshot generation procedure. Two different measures of this approximation error are utilized at two different stages in the snapshot generation algorithm, the average relative L_2-error, which is defined as:

$$E_{L_2}^{ave}(ROM) = \frac{1}{a} \sum_{k=1}^{a} \frac{\left\| R^{FOM}(\vec{x}, \vec{\gamma}_k) - R^{ROM}(\vec{x}, \vec{\gamma}_k) \right\|_{L_2(\Omega)}}{\left\| R^{FOM}(\vec{x}, \vec{\gamma}_k) \right\|_{L_2(\Omega)}}, \tag{3.9}$$

and the maximum relative L_∞-error, which is defined as:

$$E_{L_\infty}^{max}(ROM) = \underset{k \in [1,a]}{\text{Max}} \frac{\left\| R^{FOM}(\vec{x}, \vec{\gamma}_k) - R^{ROM}(\vec{x}, \vec{\gamma}_k) \right\|_{L_\infty(\Omega)}}{\left\| R^{FOM}(\vec{x}, \vec{\gamma}_k) \right\|_{L_\infty(\Omega)}}, \tag{3.10}$$

where a is the number of response fields in the ROM test set, R^{FOM} is the response field simulated with the full-order model, R^{ROM} is the response field simulated with the ROM, and $\|\cdot\|_{L_2(\Omega)}$ and $\|\cdot\|_{L_\infty(\Omega)}$ are the standard L_2 and L_∞ norms, respectively. In addition, two error tolerance values are set by the user, E_{Level}^{tol} (i.e., the level error tolerance), which corresponds to the average relative L_2-error and is used to determine the final level of the nested grid to generate the snapshots, and E_{Local}^{tol} (i.e., the local error tolerance), which corresponds to the maximum relative L_∞-error and is used during the local refinement process. Therefore, the first step in the snapshot generation procedure is to create the ROM test set by randomly generating a set of parameter sets and calculating the associated response fields with the full-order simulation. Then, an initial set of snapshots is created based on a nested grid with a selected level (this level could typically be chosen as an arbitrarily small number, such as 1) and an ROM is created from this set of snapshots. The level of the nested grid is iteratively increased, with the corresponding new parameter sets evaluated with the full-order model and the ROM updated after each iteration until the average relative L_2-error of the ROM computed with the ROM test set is below the level error tolerance. Lastly, the local refinement procedure iteratively generates additional snapshots by sampling a hypercube with a user-defined sampling procedure (e.g., a uniform grid) in the parameter space of user-defined relative length (l) centered at the parameter set values from the ROM test set corresponding to the maximum relative L_∞-error ($\vec{S}$), and the ROM is again updated after each iteration until the maximum relative L_∞-error is below the local error tolerance.

3.3.3 Computationally Efficient Stochastic Inverse Problem Solution Procedure

Putting all of the components together, the complete process for computationally efficient approximation of inverse problem solutions involving SPDEs is as follows:

Step 1: Create a reduced-order model for the SPDE of interest using a traditional (full-order) numerical solution technique (e.g., finite element anlaysis) to adaptively generate an optimal set of snapshots (Section 3.3.2).

Step 2: Create a surrogate model for the SPDE of interest that will estimate the system response given inverse problem and uncertain system parameters using the reduced-order model with the sparse grid collocation method (Section 3.3.1).

Step 3: Apply the computational inverse problem solution procedure to estimate the solution to the inverse problem by minimizing the difference between the measured/target system response and the response estimated by the surrogate model (Equation (3.1)).

3.4 EXAMPLE AND DISCUSSION

Two numerical case studies were considered to investigate the potential capabilities of the presented approach for creating a ROM using an adaptive nested grid sampling strategy and utilizing this ROM to construct a surrogate model to be used in an inverse problem solution strategy of a system with uncertainty. The objective of the first case study was to inversely calculate the unknown localized reduction in stiffness of a structure from simulated frequency response function based nondestructive testing. Alternatively, the objective of the second case study was to inversely calculate the temperature-dependent thermal conductivity of a solid from simulated thermal testing.

For both case studies standard Galerkin finite element analysis [71] was used to simulate the "experimental" measurements and to generate the snapshots for the ROM construction. For all examples, the Gauss Patterson approach [82] was chosen to define the grid points for both the snapshot selection process to create ROMs and the sparse grid surrogate model

method. The ROM test sets for calculating the error norms of the ROM were comprised of 50 randomly generated response field snapshots, the level error tolerance was defined as $E_{Level}^{tol} = 5\%$, and the local error tolerance was defined as $E_{Local}^{tol} = 1\%$ for both example. Gauss Patterson grids were used for the sparse grids with an initial level of one, and the local refinement process for the ROM generation adaptively defined the hypercube length (l) as the euclidean distance in the parameter space between the parameter set corresponding to $E_{L_\infty}^{max}(ROM)$ ($\vec{S}$) and the next nearest parameter set from the current set of snapshots used to create the ROM. A genetic algorithm (GA) (a stochastic optimization algorithm) [28] was applied to approximate the inverse problem solutions for all examples (as described in Section 3.3). For simplicity, standard GA parameters were utilized and the stopping criteria was set to be well in excess of the actual convergence of the GA population to ensure that the optimization process was as successful as possible for each trial, and therefore, did not bias the results. An important point is that although a GA provides significant global search capabilities, a GA would typically be computationally excessive for problems such as this, since GAs usually require a relatively large number of function evaluations to converge to a solution. However, the use of surrogate modeling herein allows even a GA to be applied with relatively low overall computational expense for the inverse solution process. An addition note is that to add some amount of realism to the examples and to partially relieve the inverse crime inherent in simulated experiments, 1% Gaussian white noise was added to all simulated experimental responses prior to applying the inverse characterization procedure as:

$$R^{mes} = R_0^{mes}(1 + 0.01\aleph) , \qquad (3.11)$$

where R_0^{mes} is the original simulated test response without noise and $\aleph$ is a normally distributed random variable with zero mean and unit variance.

3.4.1 Stiffness Characterization from Frequency Response Testing

The first numerical example was based upon characterization of the stiffness of a solid from frequency response testing and consisted of a $1m \times 1m \times 0.01m$ aluminum plate, that was fixed along the bottom and free to displace on the remaining three sides. Figure 3.1 shows

a schematic of the plate and the simulated nondestructive test used to perform the inverse material characterization. For the simulated test, an actuator was assumed to be represented by a harmonic pressure force of $1kPa$ applied to a $5cm$ region normal to the top surface that excited the structure to steady state at 10 equally spaced excitation frequencies between 100 to 1000 Hz, while the resulting harmonic displacement amplitudes were measured at nine "sensor" locations for each excitation frequency. The horizontal position of the actuator was assumed to be the main source of uncertainty for this inverse problem example, and was assumed to be described by a uniformly distributed random variable $X_F \sim U(0.6, 0.8)m$.

3.4.1.1 Forward Problem and Reduced-Order Modeling:

The structure was assumed to behave linearly elastically with respect to the nondestructive testing (NDT) and represented by steady-state dynamic solid mechanics. Therefore, the SPDE and boundary conditions governing the behavior of the structure can be written as:

$$\nabla \cdot \sigma(\vec{x}, \omega, \vec{\varphi}) + \omega^2 \rho \vec{u}(\vec{x}, \omega, \vec{\varphi}) = \vec{0}, \quad \forall \, \vec{x} \in \Omega,$$
$$\sigma(\vec{x}, \omega, \vec{\varphi}) \cdot \vec{n}(\vec{x}) = \vec{G}(\vec{x}, \omega, \vec{\varphi}), \quad \forall \, \vec{x} \in \Gamma_G, \tag{3.12}$$
$$\vec{u}(\vec{x}, \omega) = \vec{u}^0(\vec{x}, \omega), \quad \forall \, \vec{x} \in \Gamma_u,$$

where σ is the stress tensor, ω is the excitation frequency, $\vec{\varphi}$ is again the vector of both the unknown/inverse problem parameters (stiffness distribution parameters for this example) and the uncertain system parameters (actuation location for this example), ρ is the density, $\vec{u}$ is the displacement vector, $\vec{n}$ is the unit normal to the surface, $\vec{G}$ is the applied traction vector, $\vec{u}^0$ is the vector of applied displacement boundary conditions, Ω is the domain of the structure, Γ_G is the portion of the domain boundary with applied traction boundary conditions (which is uncertain for this example), and Γ_u is the portion of the domain boundary with applied displacement boundary conditions. In addition, the response of the thin plate was assumed to obey the plane stress condition. The material parameters of the plate were based upon standard values for aluminum, with a Poisson's ratio of $\nu = 0.3$ and density of $\rho = 2700 \ kg/m^3$. The elastic modulus distribution was assumed to be the primary unknown
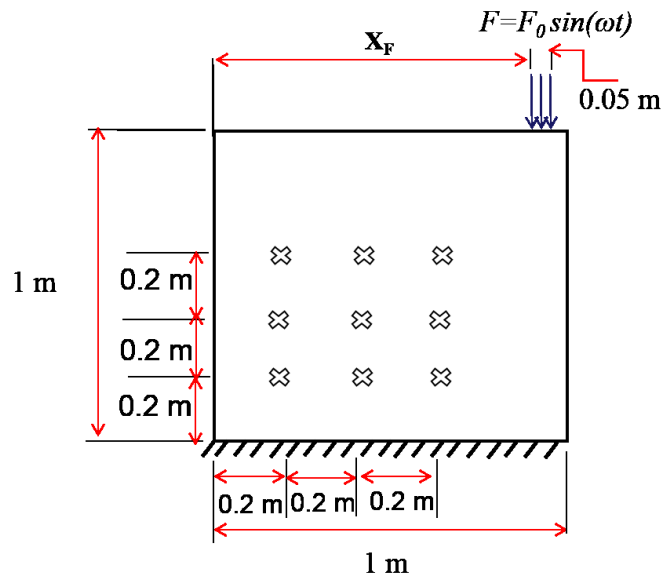
Figure 3.1: Schematic for the first example of stiffness characterization of a plate from frequency response testing, displaying the sensor locations (x-marks) and the actuator location (X_F).

of the inverse problem, but for simplicity, the distribution was assumed to be known to be localized (as could be potentially applicable for damage characterization problems) with a base value of 69 GPa, and defined by a radial basis function (RBF) representation as:

$$E(\vec{x}) = \left[1 - D \cdot \exp\left(-\frac{\|\vec{x} - \vec{\epsilon}\|^2}{c}\right)\right] \times 69 \; GPa, \tag{3.13}$$

where $\|.\|$ represents the standard l_2-norm, D is the Young's modulus percent reduction, $\vec{\epsilon}$, is the center of the RBF (i.e., localized stiffness change), and c is the breadth of the RBF. For the ROM and surrogate model generation and the inverse characterization process, the material parameters were assumed to be bounded as follows: $D \in [0, 1]$, $\vec{\epsilon} \in [0, 1] \times [0, 1]$, and $c \in [0, 0.1]$.

Applying the Galerkin projection described in Section 3.3.2 to the governing equations (Equation 3.7) produces the ROM for the steady-state dynamic solid mechanics problem as:

$$\begin{aligned}
\int_\Omega \nabla\vec{\phi}_c(\vec{x}) : &\left(\mu\left[\sum_{i=1}^m \alpha_i(\omega, \vec{\varphi})\nabla\vec{\phi}_i(\vec{x}) + \left(\sum_{i=1}^m \alpha_i(\omega, \vec{\varphi})\nabla\vec{\phi}_i(\vec{x})\right)^T\right]\right) d\vec{x} \\
&+ \int_\Omega \nabla\vec{\phi}_c(\vec{x}) : \left(\lambda\left(\nabla \cdot \sum_{i=1}^m \alpha_i(\omega, \vec{\varphi})\vec{\phi}_i(\vec{x})\right)I\right) d\vec{x} \\
&- \int_\Omega \omega^2\rho\vec{\phi}_c(\vec{x}) \cdot \left(\sum_{i=1}^m \alpha_i(\omega, \vec{\varphi})\vec{\phi}_i(\vec{x})\right) d\vec{x} \\
&- \int_{\Gamma_G} \vec{\phi}_c(\vec{x}) \cdot \vec{G}(\vec{x}, \omega, \vec{\varphi})d\vec{x} = 0, \quad \text{for } c = 1...m,
\end{aligned} \tag{3.14}$$

where I is the identity tenor, and the Lamé constants can be expressed in terms of the elastic modulus and Poisson's ratio as:

$$\lambda = \frac{E(\vec{x})\nu}{(1 - 2\nu)(1 + \nu)} \tag{3.15}$$

$$\mu = \frac{E(\vec{x})}{2(1 + \nu)}. \tag{3.16}$$

The POD procedure with adaptive snapshot generation described in Section 3.3.2 was applied to determine the basis for the above ROM. As such, snapshot displacement fields were generated with full-order analyses based upon variations in the input parameters of the

RBF (D, C and $\vec{\epsilon}$), the actuation location (X_F), and excitation frequency (ω). The adaptive nested grid snapshot generation algorithm converged at a total of 97 snapshots, which were used to create the ROM that would be applied for the surrogate model generation.

An intermediate test was performed first, in which the response approximation capabilities of an ROM created with the adaptive strategy presented was compared to the approximation capabilities of a "baseline" ROM created with an equivalent number (i.e., 97) of snapshots that were entirely randomly generated from the space of input parameters (as has often been the default snapshot creation strategy in the literature). The average relative L_2-error and the maximum relative L_∞-error (as defined previously in 3.9 and 3.10, respectively) between both ROMs and a set of 50 test response fields that were randomly generated (and different than the snapshot sets used to generate the ROMs) were calculated. The two error values (L_2 and L_∞) for the adaptively generated ROM were 1.2% and 1.9%, respectively, while the error values for the baseline ROM were 2.11% and 2.14%, respectively. Thus, the use of the adaptive nested grid snapshot generation strategy improved the accuracy of the resulting ROM by 40% in terms of the average relative L_2-error and 10% in terms of the L_∞-error in comparison to a common random generation approach.

3.4.1.2 Surrogate Modeling: In order to construct a sparse grid approximation of the displacement with respect to the vector of unknown/inverse problem parameters and the vector of uncertain system parameters (parameters of the RBF, excitation frequency, and the location of the actuator) as described in Section 3.3.1, a 6 dimensional level 5 sparse grid, which required $1,345$ evaluations of the ROM, was found to be suitable to approximate the displacement fields. Note that the computing cost (in terms of analysis time) of the ROM was approximately 10% of the cost of the equivalent full-order model, and therefore, the overall cost of creating the surrogate model was approximately 10% of what would have been required with a full-order model.

3.4.1.3 Inverse Problem Results: The objective of the inverse problem for this first example was to determine the statistics of the elastic modulus distribution, and therefore the RBF parameters (D, c, and $\vec{\epsilon}$), with respect to the nondestructive test with the uncertain

location of the actuation (X_F). The objective functional used for the optimization-based inverse solution procedure in terms of the nine displacement measurement locations ($\{\vec{X}_{Si}\}_{i=1}^9$) at the 10 excitation frequencies was cast as:

$$J(D, c, \vec{\epsilon}) = \sum_{i=1}^{9} \sum_{j=1}^{10} \frac{\left(R^{mes}(\vec{X}_{Si}, \omega_j) - R^{sim}(\vec{X}_{Si}, \omega_j; D, c, \vec{\epsilon}, X_F)\right)^2}{\left(R^{mes}(\vec{X}_{Si}, \omega_j)\right)^2}, \qquad (3.17)$$

where R^{mes} is the simulated experimentally measured response (i.e., target response) and R^{sim} is the response estimate simulated with the surrogate model for a given estimate of the inverse problem solution and the uncertain parameter. To estimate the statistical moments of the inverse problem solution, the optimization-based solution procedure was repeated 20 times, each time with a different randomly generated value of the actuator location (within the given bounds) assumed within the surrogate model estimate of the system response to be compared to the simulated experimental measurements. Also note that the actuator location used to generate the simulated experimental measurements was randomly selected, but fixed for all trials (as would be the case in reality). 20 was chosen arbitrarily as the number of trials, since the accuracy of the statistics of the solution was considered less important than showing that the surrogate model approach was capable of estimating these solutions (nearly) as accurately as a traditional (full-order) model, but with a fraction of the computational expense. For each trial the stopping criteria for the GA optimization process to estimate the material parameters was set as a maximum of $7,000$ functional evaluations.

Table 3.1 shows the mean (the first moment) and variance (the second central moment) of the RBF parameters estimated by the inverse solution process. Table 3.1 also shows the mean and variance of the measurement error corresponding to the parameter estimates with respect to the surrogate model (Equation 3.17) and the measurement error of those parameter estimates with respect to the full-order model (Equation 3.17 with the full-order model in place of the surrogate model for R^{sim}), as well as the error between the surrogate model and the full-order model (Equation 3.17 with the full-order model in place of the target response, R^{mes}) for the parameter estimates. Furthermore, the parameter values estimated produced a mean relative L_2 and L_∞ error in the estimated elastic modulus distribution in comparison to the distribution used to simulate the experimental measurements of 7.8% and

Table 3.1: Target (i.e., simulated experimental) values for the unknown damage amplitude (D), the breadth of the damage region (c), and the horizontal and vertical location of the center of the damage region (ϵ_x, ϵ_y), the mean and variance of the corresponding values estimated by the inverse characterization process for the 20 trials, and the mean and variance of the measurement error corresponding to the parameter estimates with respect to the surrogate model (SM-EXP), the measurement error with respect to the full-order model (FOM-EXP), and the error between the surrogate model and the full-order model (SM-FOM) for the first example.

	D	c	ϵ_x	ϵ_y	Relative L_2-Error		
Target Value	0.7	0.005	0.7	0.3	SM-EXP	FOM-EXP	SM-FOM
Mean	0.49	0.005	0.7	0.37	0.14	0.19	0.02
Variance	0.059	6.18×10^{-6}	0.026	0.020	0.007	0.04	0.005

49%, respectively. The resulting parameter values were consistent with the sensitivity of the system response to the uncertain system parameter, with the mean value of the breadth and horizontal location of the RBF having been accurate in comparison with the target values (i.e., those used to simulate the experimental data) and with relatively low variances. Alternatively, the amplitude and vertical location of the RBF were more sensitive to the uncertain actuator location, particularly relative to the sensitivity of the measured response to those parameters themselves, and therefore, had significantly more relative variance and lower accuracy overall. The measurement error with respect to the simulated experiment with the full-order model in place of surrogate model shows higher relative L_2-Error than the measurement error of simulated experiment with surrogate model, which is expected since the error objective functional was minimized based on surrogate model. More importantly, the difference between the surrogate and full-order models and the change in measurement error when analyzing the solutions with the full-order model rather than the surrogate model were both relatively low, providing confidence that the surrogate model was able to accu-

rately represent the system response, and thus, provide accurate estimates to the statistical moments of the inverse problem solution. This is particularly impressive when considering that the surrogate model was built using only 147 full-order analyses (97 for the ROM snapshots and 50 for the ROM test set) to then be used for 140,000 system evaluations (7,000 evaluations for each of the 20 GA trials), with those 140,000 system evaluations only requiring on the order of 1 hour of computing time on a standard PC with a 2.00 GHz processor and 4 GB RAM.

3.4.2 Conductivity Characterization from Thermal Testing

The second numerical example was based upon characterization of the thermal conductivity of a solid from temperature measurements. Figure 3.2 shows a schematic of the $0.2m \times 0.2m$ two-dimensional plate structure and the simulated thermal testing considered. The simulated thermal testing involved applying a heat flux to the top surface of the plate, with the plate having a known initial temperature of 0 throughout and the remaining three sides fixed at a temperature of 0, and the transient temperature response at 10 discrete "sensors" within the plate was measured. The applied heat flux was assumed to be the main source of uncertainty for this problem, with this uniformly applied flux assumed to be defined and known for the purposes of the inverse problem as:

$$\bar{q} = 7 \times 10^5 \times (1 + \zeta) \ \ W/m^2, \tag{3.18}$$

where the uniformly distributed random variable $\zeta \sim U(0, 1)$. Then, the test was simulated by randomly generating 40 realizations of the applied heat flux from the given distribution, and for each realization of the applied flux the resulting temperature was measured at 10 uniformly spaced points in time between $0s$ and $1s$ at each sensor to produce the first moment and second central moment of the temperature at each sensor and each time step with respect to the variable flux.
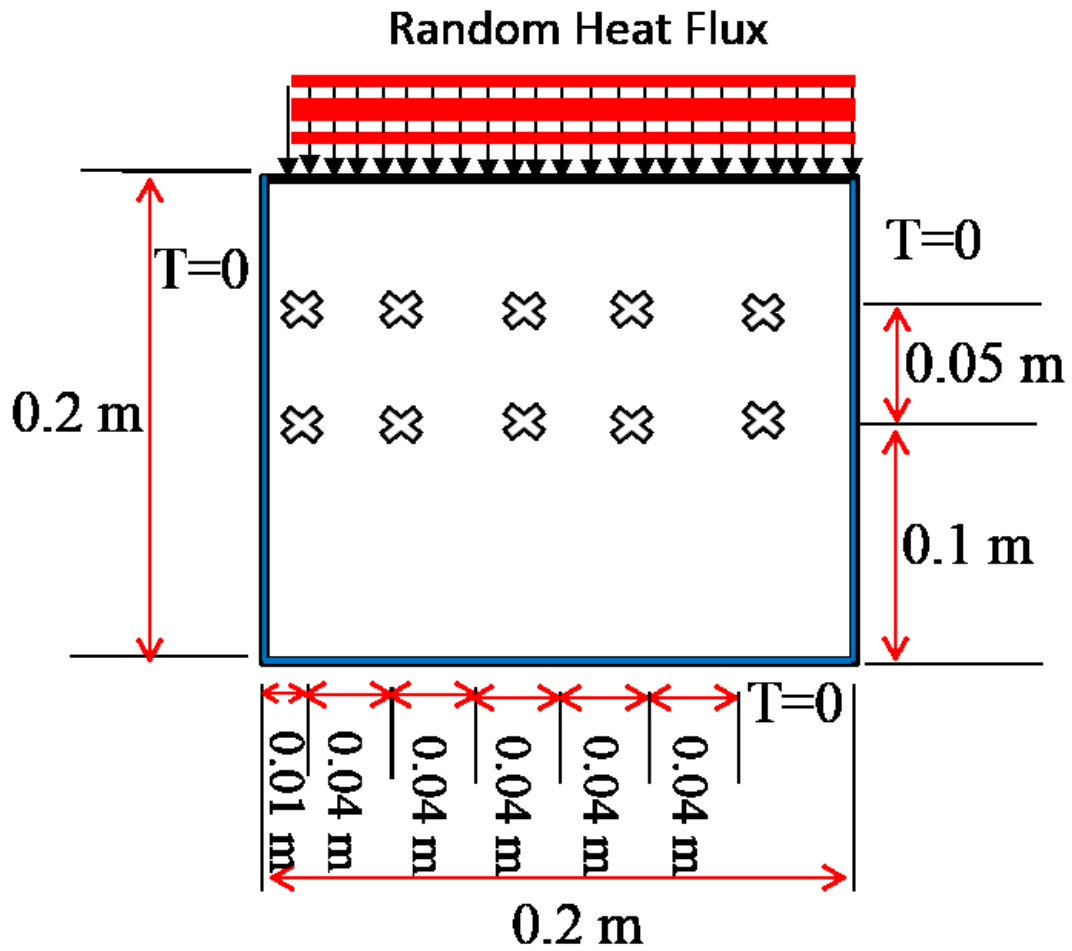
Figure 3.2: Schematic for the second example of conductivity characterization from thermal testing, displaying the sensor locations (x-marks) and the temperature and flux boundary conditions.

3.4.2.1 Forward Problem and Reduced-Order Modeling: The structure for this example was assumed to have a nonlinear transient thermal response due to a nonlinear thermal conductivity and no internal heat sources, with the SPDE and boundary conditions governing the behavior given as:

$$\rho\, C_v\, \frac{\partial T(\vec{x}, t, \vec{\varphi})}{\partial t} - \nabla \cdot [\kappa(T(\vec{x}, t, \vec{\varphi})) \cdot \nabla T(\vec{x}, t, \vec{\varphi})] = 0, \quad \forall\, \vec{x} \in \Omega,$$

$$-(\kappa\, (T(\vec{x}, t, \vec{\varphi})) \cdot \nabla T(\vec{x}, t, \vec{\varphi})) \cdot \vec{n}(\vec{x}) = \bar{q}(\zeta), \quad \forall\, \vec{x} \in \Gamma_q,$$

$$T(\vec{x}, t, \vec{\varphi}) = 0, \quad \forall\, \vec{x} \in \Gamma_T,$$

$$T(\vec{x}, t = 0, \vec{\varphi}) = 0, \quad \forall\, \vec{x} \in \Omega,$$

$$(3.19)$$

where T is the temperature, $t \in [0, 1]s$ is the time, ρ is the density, C_v is the specific heat, $\kappa(T)$ is the temperature-dependent thermal conductivity, $\vec{\varphi}$ is again the vector of both the unknown/inverse problem parameters (heat conductivity parameters for this example) and the uncertain system parameters (heat flux magnitude for this example), $\vec{n}$ is the unit normal to the surface, Ω is the domain of the structure, Γ_q is the portion of the domain boundary with applied heat flux boundary conditions, and Γ_T is the portion of the domain boundary with applied temperature boundary conditions. The specific material parameters were based on those utilized in [7] (with some minor modification to the function used to define the thermal conductivity), with a density of $\rho = 7850\ kg/m^3$ and specific heat of $C_v = 419\ J/(kg \cdot^o C)$. The temperature-dependent thermal conductivity $\kappa(T)$ was assumed to be the primary unknown of the inverse problem and defined in terms of four scalar coefficients in the following form:

$$\kappa\, (T(\vec{x}, t, \vec{\varphi})) = c_3 T^3(\vec{x}, t, \vec{\varphi}) + c_2 T^2(\vec{x}, t, \vec{\varphi}) + c_1 T(\vec{x}, t, \vec{\varphi}) + c_0. \quad (3.20)$$

For the ROM and surrogate model generation and the inverse characterization process, the four material parameters were assumed to be bounded as follows: $c_0 \in [420, 980]$, $c_1 \in [1.8 \times 10^{-3}, 4.2 \times 10^{-3}]$, $c_2 \in [1.2 \times 10^{-3}, 2.8 \times 10^{-3}]$, and $c_3 = [0.66 \times 10^{-3}, 1.55 \times 10^{-3}]$.

Applying the Galerkin projection described in Section 3.3.2 to the governing equations (Equation 3.19) produces the ROM for the nonlinear transient heat transfer problem as:

$$\rho\ C_v\ \frac{\partial \alpha_c(\vec{\varphi}, t)}{\partial t} + c_0 \sum_{i=1}^{m} \alpha_i(\vec{\varphi}, t) \int_{\Omega} \nabla\phi_i(\vec{x}) \cdot \nabla\phi_c(\vec{x}) d\vec{x}$$

$$+ c_1 \int_{\Omega} \left(\sum_{j=1}^{m} \alpha_j(\vec{\varphi}, t)\phi_j(\vec{x}) \right) \cdot \sum_{i=1}^{m} \alpha_i(\vec{\varphi}, t) \nabla\phi_i(\vec{x}) \cdot \nabla\phi_c(\vec{x}) d\vec{x}$$

$$+ c_2 \int_{\Omega} \left(\sum_{j=1}^{m} \alpha_j(\vec{\varphi}, t)\phi_j(\vec{x}) \right)^2 \cdot \sum_{i=1}^{m} \alpha_i(\vec{\varphi}, t) \nabla\phi_i(\vec{x}) \cdot \nabla\phi_c(\vec{x}) d\vec{x} \qquad (3.21)$$

$$+ c_3 \int_{\Omega} \left(\sum_{j=1}^{m} \alpha_j(\vec{\varphi}, t)\phi_j(\vec{x}) \right)^3 \cdot \sum_{i=1}^{m} \alpha_i(\vec{\varphi}, t) \nabla\phi_i(\vec{x}) \cdot \nabla\phi_c(\vec{x}) d\vec{x}$$

$$- \int_{\Gamma_q} \phi_c(\vec{x})\overline{q}\ d\vec{x} = 0, \quad \text{for} \ \ c = 1...m,$$

with

$$\alpha_c(\vec{\varphi}, t = 0) = \int_{\Omega} T_0 \cdot \phi_c(\vec{x}) d\vec{x}, \quad \text{for} \ \ c = 1...m. \qquad (3.22)$$

The snapshot temperature fields generated with full-order analyses using the adaptive snapshot generation algorithm were based upon variations in the thermal conductivity parameters (c_0, c_1, c_2, and c_3) and the heat flux amplitude parameter (ζ). Alternatively, for simplicity, the time sampling was fixed for the snapshot generation, with three times generated for each conductivity and heat flux combination: $t = 0.3s$, $t = 0.6s$, and $t = 0.9s$. The adaptive nested grid snapshot generation algorithm converged at a total of 33 transient full-order analyses to form the snapshot set used to create the ROM.

Again, an intermediate test was performed first, in which the response approximation capabilities of an ROM created with the adaptive strategy presented was compared to the approximation capabilities of a baseline ROM created with an equivalent number (i.e., 50) of snapshots that were entirely randomly generated from the space of input parameters. The average relative L_2-error and the maximum relative L_∞-error between both ROMs and a set of 50 test response fields that were randomly generated were calculated. The two error values (L_2 and L_∞) for the adaptively generated ROM were 0.9% and 1.1%, respectively, while the error values for the baseline ROM were 2% and 2.2%, respectively. Thus, the use of

the adaptive nested grid snapshot generation strategy improved the accuracy of the resulting ROM by 55% in terms of the average relative L_2-error and 50% in terms of the L_∞-error in comparison to a common random generation approach for this second example.

3.4.2.2 Surrogate Modeling: A 6 dimensional level 5 sparse grid was used to construct a suitably accurate surrogate model approximation of the temperature response with respect to the thermal conductivity parameters, the heat flux parameter, and the time, which required $1,345$ evaluations of the ROM. Similarly as the previous example, the computing cost of the ROM was approximately 5% compared to that of the full-order model used to create the ROM, and therefore, the overall cost of constructing the sparse grid surrogate model was 5% of the computing cost that would have been required to use the full-order model only.

3.4.2.3 Inverse Problem Results: The objective of the inverse problem for this second example was to determine the parameters of the temperature-dependent thermal conductivity function (c_0, c_1, c_2 and c_3) with respect to the simulated thermal test that produced the two statistical moments (i.e., mean and variance) of the temperature at each sensor location ($\{\vec{X}_{Si}\}_{i=1}^{10}$) at 10 uniformly spaced points in time between $0s$ and $1s$ ($\{t_i\}_{i=1}^{10}$) with respect to the uncertain applied flux parameter (ζ). Therefore, the objective functional used for the optimization-based inverse solution procedure was defined as:

$$ J = \sum_{i=1}^{10} \sum_{j=1}^{10} \sum_{k=1}^{2} \left| \frac{\left\langle T^{mes}(\vec{X}_{Si}, t_j) \right\rangle_k - \left\langle T^{sim}(\vec{X}_{Si}, t_j; c_0, c_1, c_2, c_3, \zeta) \right\rangle_k}{\left\langle T^{mes}(\vec{X}_{Si}, t_j) \right\rangle_k} \right| \tag{3.23} $$

where T^{mes} is the simulated experimentally measured response, T^{sim} is the response estimate simulated with the surrogate model for a given estimate of the inverse problem solution and the uncertain parameter, $\langle . \rangle_1$ represents the first moment operator, $\langle . \rangle_2$ represents the second central moment operator, and $|.|$ is the absolute value operator. Similarly to the approach that was used to generate the simulated experimental data, the moments of the temperature response were estimated with the surrogate model during the optimization process (i.e., at each iteration) by randomly generating 40 realizations of the applied heat flux parameter, evaluating the surrogate model with each realization (given values of the thermal conductivity

Table 3.2: Target (i.e., simulated experimental) values for the heat conductivity parameters (c_0, c_1, c_2 and c_3) and the corresponding values estimated by the inverse characterization process, as well as the respective relative error for east estimated parameter.

	c_0	c_1	c_2	c_3
Target Value	650	2.5×10^{-3}	2.5×10^{-3}	1.2×10^{-3}
Estimated Value	640	1.98×10^{-3}	2.46×10^{-3}	1.12×10^{-3}
Relative Error	1.5%	20.8%	1.6%	6.7%

parameters and the time), and then estimating the moments from the results. The stopping criteria for the GA optimization process to estimate the material parameters for this example was set as a maximum of $40,000$ evaluations of the error functional.

Table 3.2 shows the thermal conductivity parameters used to simulate the experimental measurements (i.e., the target conductivity parameters), the thermal conductivity parameters estimated with the inverse solution process, and the relative error between each target and estimated parameter. More importantly, Figure 3.3 shows a plot of the temperature-dependent thermal conductivity that corresponds to the parameters used to simulate the experimental measurements (i.e., the target conductivity function) compared to the thermal conductivity corresponding to the parameters estimated through the inverse solution procedure. These results clearly indicate that the inverse procedure utilizing the computationally efficient surrogate model was able to accurately estimate temperature-dependent thermal conductivity, with the approximate relative L_2-error in the thermal conductivity being 0.38%. More specifically, the surrogate model was capable of successfully capturing the relationship between the temperature response and the uncertain applied flux for the potential variations in the thermal conductivity with sufficient accuracy to guide the optimization-based inverse solution procedure through the parameter space to an accurate solution. Similarly to the previous example, the surrogate model also provided a dramatic decrease in the computational expense compared to if the full-order model or reduced-order
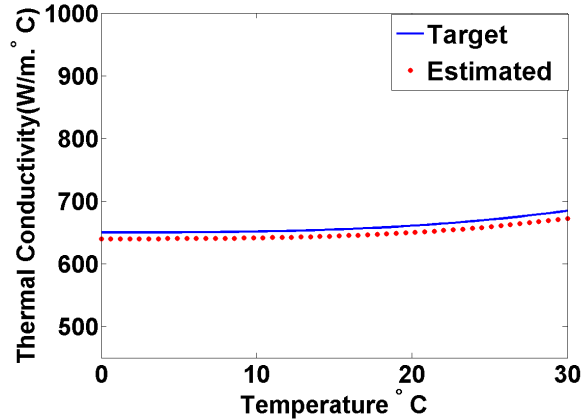
Figure 3.3: Target (i.e., simulated experimental) temperature-dependent thermal conductivity and the thermal conductivity estimated by the inverse characterization process (Estimated).

model had been used directly. For this second example, the surrogate model was built using only 83 full-order analyses (33 for the ROM snapshots and 50 for the ROM test set) to then be used for 40,000 system evaluations, which required on the order of 30 minutes of computing time on a standard PC with a 2.00 GHz processor and 4 GB RAM.

3.5 CONCLUSION

A generally applicable approach was presented for creating a computationally efficient polynomial approximation (i.e., surrogate model) of a system response with respect to any designated unknown parameters, including parameters that may be considered to have significant uncertainty and/or parameters that are entirely unknown and sought to be determined through an inverse solution procedure. To enhance the overall efficiency of the approach, a novel algorithm was included as an intermediate step for creating a reduced-basis type reduced-order model of the system of interest based upon a technique to use nested grids to adaptively generate a data ensemble that is representative of the potential system response

with respect to the unknown/uncertain parameters. The overall approach would then use this computationally efficient ROM to create the surrogate model rather than a full-order model (e.g., traditional finite element analysis) at a substantial computational savings. This approach to generate an ROM was shown to provide a more accurate representation of the system of interest in comparison to a commonly used approach of randomly generating the response field ensemble. The overall surrogate modeling approach was then evaluated through numerically simulated example inverse problems based on characterization of material properties for two different systems, involving solid mechanics and heat transfer, respectively. Not only did the two examples consider different physical processes, but they also consider two different ways that uncertainty could be present and significant within an inverse problem application. The first example showed that the surrogate modeling approach could be used to computationally efficiently and accurately estimate the statistical moments of the parameters for an unknown stiffness distribution for a dynamically tested solid with uncertainty in the applied actuation. Lastly, the surrogate modeling approach was shown to be able to provide a single estimate, again both efficiently and accurately, of the parameters for an unknown temperature-dependent thermal conductivity for a solid in which the inverse problem objective was to match the statistical moments of the measured temperature field given an uncertain applied heat flux.

4.0 CURRENT CAPABILITIES AND FUTURE DIRECTIONS

A computational inverse problem solution approximation framework has been developed that significantly improves the efficiency and accuracy of computational inverse mechanics for both the setup and solution process of inverse problems with applications in material characterization. The framework is capable of improving nondestructive test (NDT) design by maximizing the measured response sensitivity in a generally applicable way for nondestructive evaluation (NDE)/material characterization problems. Through simulated examples of frequency response function-based NDT, the optimal NDT design approach was shown to provide consistently more accurate material characterization results than alternate testing techniques. This indicates the ability of the optimized NDT design to produce a substantially more solvable inverse problem. In addition, this work extended the concept of maximizing test response sensitivity to include the maximization of robustness to uncertainty of system parameters that are not part of the set to be inversely characterized with the NDT. The extended robust NDT design was shown to produced more accurate material characterization results for the NDE of structural components with epistemic uncertainty in comparison to deterministic NDT designs.

The issue of the computational expense of solving an inverse problem was addressed by developing a generally applicable algorithm for creating a low cost approximation of the physical system. More specifically, the current work is capable of substantially reducing the computational expense required to approximate the solution of a stochastic partial differential equation (PDE), particularly for the purpose of estimating the solution to an associated inverse problem. The approach combines reduced-basis reduced-order modeling with a sparse grid collocation surrogate modeling technique to estimate the response of the system of interest with respect to both the inverse problem unknowns and the uncertain

system parameters. This computationally efficient approach was shown through simulated examples involving both solid mechanics and heat transfer to provide accurate solution estimates to inverse problems for systems represented by stochastic PDEs with a fraction of the typical computational cost. In addition, a novel, generally applicable algorithm is integrated for adaptive generation of a data ensemble, which is then used to create a reduced-order model (ROM) to estimate the desired system response.

However, certain extensions need to be made in order to improve the computational efficiency and applicability of the developed framework for large scale systems and systems with significant measurement noise. More specifically, since calculating the measured response sensitivity due to the unknown material properties is computationally expensive, adjoint methods can instead be used to calculate the sensitivity information with respect to unknown material properties with a fraction of the computational time that is needed by traditional methods (as were used herein). The capability of the developed framework can also be extended to include higher levels of noise in measurements (e.g., aleatoric uncertainties) by using Bayesian inference methods, which are powerful tools for modeling various information sources and quantifying uncertainty of a model. In order to generate a sufficient number of samples to construct the posterior distribution to be used in Bayesian inference approach, Markov chain Monte Carlo (MCMC) methods require sequential evaluations of the posterior probability density at many different points in the parameter space. This can be a computationally expensive process. Alternatively, the developed sparse grid approximation can be used to calculate the solution of the forward model used to define the likelihood function and provide near real time estimation of the state of the system based on measurement data.

APPENDIX A

PROPER ORTHOGONAL DECOMPOSITION

A.1 OBJECTIVE

Apply the proper orthogonal decomposition (POD) method to derive an orthogonal basis that is optimal in some sense to represent a given system provided with an associated set of representative system response fields.

A.2 METHODS

The problem to determine the POD basis can be cast as an optimization problem to determine the set of m modes $\{\vec{\phi_i}(\vec{x})\}_{i=1}^{m}$ given a set of n system response fields (referred to as snapshots in the context of POD) $\{\vec{u}(\vec{x}, \vec{\gamma}_k)\}_{k=1}^{n}$, from a set of various input parameters of interest $\{\vec{\gamma}_k\}_{k=1}^{n}$, such that:

$$\underset{\{\vec{\phi_i}(\vec{x})\}_{i=1}^{m} \in L_2(\Omega)}{\text{Minimize}} \left\langle \|\vec{u}(\vec{x}, \vec{\gamma}_k) - \hat{\vec{u}}(\vec{x}, \vec{\gamma}_k)\|_{L_2(\Omega)}^2 \right\rangle, \tag{A.1}$$

where:

$$\langle \vec{u_k} \rangle = \frac{1}{n} \sum_{k=1}^{n} \vec{u_k}, \tag{A.2}$$

$$\|\vec{u}(\vec{x})\|_{L_2(\Omega)}^2 = (\vec{u}(\vec{x}), \vec{u}(\vec{x})), \tag{A.3}$$

89

$$(\vec{u}(\vec{x}), \vec{v}(\vec{x})) = \int_{\Omega} \vec{u}(\vec{x}) \cdot \vec{v}(\vec{x}) d\vec{x}, \tag{A.4}$$

and assuming an orthogonal basis, the best approximation can be defined by the projection onto the basis as:

$$\hat{\vec{u}}(\vec{x}, \vec{\gamma}_k) = \sum_{i=1}^{n} \frac{\left(\vec{\phi}_i(\vec{x}), \vec{u}(\vec{x}, \vec{\gamma}_k) \right)}{\|\vec{\phi}_i(\vec{x})\|_{L_2(\Omega)}^2} \vec{\phi}_i(\vec{x}). \tag{A.5}$$

Through several manipulations, including applying the method of snapshots, the POD optimization problem defined by A.1 can be transformed into the following n-dimensional eigenvalue problem (see [19] and the references therein for additional details on the POD formulation):

$$\frac{1}{n} \sum_{k=1}^{n} A_{jk} C_k = \lambda C_j, \tag{A.6}$$

where

$$A_{jk} = \int_{\Omega} \vec{u}(\vec{x}, \vec{\gamma}_j) \cdot \vec{u}(\vec{x}, \vec{\gamma}_k) d\vec{x}, \tag{A.7}$$

An optimal set of as many as n orthogonal basis functions (i.e., POD modes) can then be determined from the solution of the above eigenvalue problem by:

$$\vec{\phi}_i(\vec{x}) = \frac{1}{\lambda^{(i)} n} \sum_{k=1}^{n} \vec{u}(\vec{x}, \vec{\gamma}_k) C_k^{(i)}, \quad \text{for } i = 1, 2, ..., n, \tag{A.8}$$

where $C_k^{(i)}$ is the kth component of the ith eigenvector from the solution of A.6 and $\lambda^{(i)}$ is the corresponding eigenvalue. $\lambda^{(i)}$ is often considered a measure of the "usefulness" of the corresponding mode $(\vec{\phi}_i(\vec{x}))$ for approximating the given dataset of potential solution fields. Therefore, a common procedure (as was done herein) is to only use the m modes with the highest corresponding eigenvalues, with $m < n$, for any subsequent solution approximation, and the remaining modes are discarded (a typical heuristic is to use the set with corresponding eigenvalues that represent around 99% of the total sum of the n eigenvalues).

BIBLIOGRAPHY

[1] Swagato Acharjee and Nicholas Zabaras. A proper orthogonal decomposition approach to microstructure model reduction in rodrigues space with applications to optimal control of microstructure-sensitive properties. *Acta Materialia*, 51(18):5627–5646, 2003.

[2] M.A. Aguilo, W. Aquino, J.C. Brigham, and M. Fatemi. An inverse problem approach for elasticity imaging through vibroacoustics. *Medical Imaging, IEEE Transactions on*, 29(4):1012–1021, 2010.

[3] M.A. Aguilo, W. Aquino, J.C. Brigham, and M. Fatemi. An inverse problem approach for elasticity imaging through vibroacoustics. *Medical Imaging, IEEE Transactions on*, 29(4):1012–1021, 2010.

[4] R.A. Albanese, H.T. Banks, and J.K. Raye. Nondestructive evaluation of materials using pulsed microwave interrogating signals and acoustic wave induced reflections. *Inverse Problems*, 18(6):1935, 2002.

[5] Marcílio Alves, Jilin Yu, and Norman Jones. On the elastic modulus degradation in continuum damage mechanics. *Computers & Structures*, 76(6):703–712, 2000.

[6] W. Aquino and J.C. Brigham. Self-learning finite elements for inverse estimation of thermal constitutive models. *International journal of heat and mass transfer*, 49(15):2466–2478, 2006.

[7] W Aquino, JC Brigham, CJ Earls, and N Sukumar. Generalized finite element method using proper orthogonal decomposition. *International Journal for Numerical Methods in Engineering*, 79(7):887–906, 2009.

[8] C. Aristégui and S. Baste. Optimal recovery of the elasticity tensor of general anisotropic materials from ultrasonic velocity data. *The Journal of the Acoustical Society of America*, 101:813, 1997.

[9] Jeanne A Atwell and Belinda B King. Proper orthogonal decomposition for reduced basis feedback controllers for parabolic equations. *Mathematical and computer modelling*, 33(1):1–19, 2001.

[10] B. Audoin. Non-destructive evaluation of composite materials with ultrasonic waves generated and detected by lasers. *Ultrasonics*, 40(1):735–740, 2002.

[11] M. Azarbayejani, AI El-Osery, K.K Choi, and M.R. Taha. A probabilistic approach for optimal sensor allocation in structural health monitoring. *Smart Materials and Structures*, 17(5):055019, 2008.

[12] Ivo Babuška, Fabio Nobile, and Raul Tempone. A stochastic collocation method for elliptic partial differential equations with random input data. *SIAM review*, 52(2):317–355, 2010.

[13] Ivo Babuska, Fabio Nobile, and Raul Tempone. A stochastic collocation method for elliptic partial differential equations with random input data. *SIAM review*, 52(2):317–355, 2010.

[14] Ivo Babuska, Raúl Tempone, and Georgios E Zouraris. Galerkin finite element approximations of stochastic elliptic partial differential equations. *SIAM Journal on Numerical Analysis*, 42(2):800–825, 2004.

[15] Volker Barthelmann, Erich Novak, and Klaus Ritter. High dimensional polynomial interpolation on sparse grids. *Advances in Computational Mathematics*, 12(4):273–288, 2000.

[16] O. Begambre and JE Laier. A hybrid particle swarm optimization–simplex algorithm (psos) for structural damage identification. *Advances in Engineering Software*, 40(9):883–891, 2009.

[17] Sébastien Boyaval, Claude Le Bris, Tony Lelièvre, Yvon Maday, Ngoc Cuong Nguyen, and Anthony T Patera. Reduced basis techniques for stochastic problems. *Archives of Computational methods in Engineering*, 17(4):435–454, 2010.

[18] J.C. Brigham and W. Aquino. Surrogate-model accelerated random search algorithm for global optimization with applications to inverse material identification. *Computer Methods in Applied Mechanics and Engineering*, 196(45):4561–4576, 2007.

[19] J.C. Brigham and W. Aquino. Inverse viscoelastic material characterization using pod reduced-order modeling in acoustic–structure interaction. *Computer Methods in Applied Mechanics and Engineering*, 198(9):893–903, 2009.

[20] John C Brigham and Wilkins Aquino. Inverse viscoelastic material characterization using pod reduced-order modeling in acoustic–structure interaction. *Computer Methods in Applied Mechanics and Engineering*, 198(9):893–903, 2009.

[21] S.H. Brooks. A discussion of random methods for seeking maxima. *Operations Research*, 6(2):244–251, 1958.

[22] Hans-Joachim Bungartz and Michael Griebel. Sparse grids. *Acta numerica*, 13:147–269, 2004.

[23] Rafael Castro-Triguero, Senthil Murugan, Rafael Gallego, and Michael I Friswell. Robustness of optimal sensor placement under parametric uncertainty. *Mechanical Systems and Signal Processing*, 41(1):268–287, 2013.

[24] FN Catbas, T Kijewski-Correa, and AE Aktan. Structural identification (st-id) of constructed facilities–approaches, methods and technologies for effective practice of st-id. In *Am Soc Civ Eng*, 2011.

[25] F Chinesta, A Ammar, F Lemarchand, P Beauchene, and F Boust. Alleviating mesh constraints: model reduction, parallel time integration and high resolution homogenization. *Computer methods in applied mechanics and engineering*, 197(5):400–413, 2008.

[26] J.H. Chou and J. Ghaboussi. Genetic algorithm in structural damage detection. *Computers & Structures*, 79(14):1335–1353, 2001.

[27] CL Chow and June Wang. An anisotropic theory of continuum damage mechanics for ductile fracture. *Engineering Fracture Mechanics*, 27(5):547–558, 1987.

[28] Kalyanmoy Deb, Amrit Pratap, Sameer Agarwal, and TAMT Meyarivan. A fast and elitist multi objective genetic algorithm: Nsga-ii. *Evolutionary Computation, IEEE Transactions on*, 6(2):182–197, 2002.

[29] Scott W Doebling, Charles R Farrar, Michael B Prime, et al. A summary review of vibration-based damage identification methods. *Shock and vibration digest*, 30(2):91–105, 1998.

[30] S.W. Doebling, C.R. Farrar, and M.B. Prime. A summary review of vibration-based damage identification methods. *Shock and Vibration Digest*, 30(2):91–105, 1998.

[31] Maia M Donahue, G Buzzard, Ann E Rundell, A Jayaraman, and J Hahn. Parameter identification with adaptive sparse grid-based optimization for models of cellular processes. *Methods in bioengineering: systems analysis of biological networks(Artech House, Boston/London, 2009)*, 2009.

[32] Eric B Flynn and Michael D Todd. A bayesian approach to optimal sensor placement for structural health monitoring with application to active sensing. *Mechanical Systems and Signal Processing*, 24(4):891–903, 2010.

[33] Philipp Frauenfelder, Christoph Schwab, and Radu Alexandru Todor. Finite elements for elliptic problems with stochastic coefficients. *Computer methods in applied mechanics and engineering*, 194(2):205–228, 2005.

[34] M. Friswell and J.E. Mottershead. *Finite element model updating in structural dynamics*, volume 38. Springer, 1995.

[35] M.I. Friswell. Damage identification using inverse methods. *Philosophical Transactions of the Royal Society A: Mathematical, Physical and Engineering Sciences*, 365(1851):393–410, 2007.

[36] Roger Ghanem and Pol D Spanos. *Stochastic finite elements: a spectral approach.* DoverPublications. com, 2003.

[37] D.E. Goldberg. Genetic algorithms in search, optimization, and machine learning. 1989.

[38] H.Y. Guo, L. Zhang, L.L Zhang, and J.X Zhou. Optimal placement of sensors for structural health monitoring using improved genetic algorithms. *Smart Materials and Structures*, 13(3):528, 2004.

[39] R.F. Guratzsch. *Sensor placement optimization under uncertainty for structural health monitoring systems of hot aerospace structures.* PhD thesis, Vanderbilt University, 2007.

[40] Sangbo Han and Brian Feeny. Application of proper orthogonal decomposition to structural vibration analysis. *Mechanical Systems and Signal Processing*, 17(5):989–1001, 2003.

[41] Ernesto Heredia-Zavoni and Luis Esteva. Optimal instrumentation of uncertain structural systems subject to earthquake ground motions. *Earthquake engineering & structural dynamics*, 27(4):343–362, 1998.

[42] SS Isukapalli, A Roy, and PG Georgopoulos. Efficient sensitivity/uncertainty analysis using the combined stochastic response surface method and automated differentiation: Application to environmental and biological systems. *Risk Analysis*, 20(5):591–602, 2000.

[43] D.C. Kammer. Sensor placement for on-orbit modal identification and correlation of large space structures. In *American Control Conference, 1990*, pages 2984–2990. IEEE, 1990.

[44] D.C. Kammer. Sensor set expansion for modal vibration testing. *Mechanical systems and signal processing*, 19(4):700–713, 2005.

[45] Mehrdad N Khajavi, Bahram Notghi, and Golamhassan Paygane. A multi objective optimization approach to optimize vehicle ride and handling characteristics. *World Acad. Sci. Eng. Technol*, 62:580–584, 2010.

[46] A. Khakhali, Nader Nariman-zadeh, A. Darvizeh, A. Masoumi, and B. Notghi. Reliability-based robust multi-objective crashworthiness optimisation of s-shaped box beams with parametric uncertainties. *International Journal of Crashworthiness*, 15(4):443–456, 2010.

[47] A. Khan and D. Ceglarek. Sensor optimization for fault diagnosis in multi-fixture assembly systems with distributed sensing. *Transactions-American Society Of Mechanical Engineers Journal of Manufacturing Science and Engineering*, 122(1):215–226, 2000.

[48] S.Y. Lee and S.C. Wooh. Detection of stiffness reductions in laminated composite plates from their dynamic response using the microgenetic algorithm. *Computational Mechanics*, 36(4):320–330, 2005.

[49] F Leibfritz and S Volkwein. Reduced order output feedback control design for pde systems using proper orthogonal decomposition and nonlinear semidefinite programming. *Linear algebra and its applications*, 415(2):542–575, 2006.

[50] Jean Lemaitre and Horst Lippmann. *A course on damage mechanics*, volume 2. Springer Berlin, 1996.

[51] Fei Li, Jin-an Wang, and John C Brigham. Inverse calculation of¡ i¿ i¡/i¿¡ i¿ n¡/i¿¡ i¿ s¡/i¿¡ i¿ itu¡/i¿ stress in rock mass using the surrogate-model accelerated random search algorithm. *Computers and Geotechnics*, 61:24–32, 2014.

[52] Jinglai Li and Youssef M Marzouk. Adaptive construction of surrogates for the bayesian solution of inverse problems. *arXiv preprint arXiv:1309.5524*, 2013.

[53] David J Lucia, Philip S Beran, and Walter A Silva. Reduced-order modeling: new approaches for computational physics. *Progress in Aerospace Sciences*, 40(1):51–117, 2004.

[54] D.G. Luenberger. *Optimization by vector space methods.* Wiley-Interscience, 1997.

[55] Christiane Maierhofer, Philipp Myrach, Mercedes Reischel, Henrik Steinfurth, Mathias Röllig, and Matthias Kunert. Characterizing damage in cfrp structures using flash thermography in reflection and transmission configurations. *Composites Part B: Engineering*, 57:35–46, 2014.

[56] J.E. Mottershead and M.I. Friswell. Model updating in structural dynamics: a survey. *Journal of sound and vibration*, 167(2):347–375, 1993.

[57] S. Nimityongskul and D.C. Kammer. Frequency response based sensor placement for the mid-frequency range. *Mechanical Systems and Signal Processing*, 23(4):1169–1179, 2009.

[58] Fabio Nobile, Raúl Tempone, and Clayton G Webster. A sparse grid stochastic collocation method for partial differential equations with random input data. *SIAM Journal on Numerical Analysis*, 46(5):2309–2345, 2008.

[59] J. Nocedal and S.J. Wright. *Numerical optimization.* Springer verlag, 1999.

[60] Bahram Notghi and John C Brigham. Optimal nondestructive test design for maximum sensitivity and minimal redundancy for applications in material characterization. *Smart Materials and Structures*, 22(12):125036, 2013.

[61] Bahram Notghi and John C Brigham. Optimal nondestructive test design for maximum sensitivity and minimal redundancy for applications in material characterization. *Smart Materials and Structures*, 22(12):125036, 2013.

[62] H. Ogi, K. Sato, T. Asada, and M. Hirao. Complete mode identification for resonance ultrasound spectroscopy. *The Journal of the Acoustical Society of America*, 112:2553, 2002.

[63] Ziemowit Ostrowski, Ryszard A Białecki, and Alain J Kassab. Estimation of constant thermal conductivity by use of proper orthogonal decomposition. *Computational Mechanics*, 37(1):52–59, 2005.

[64] C. Papadimitriou. Optimal sensor placement methodology for parametric identification of structural systems. *Journal of sound and vibration*, 278(4):923–947, 2004.

[65] C. Papadimitriou, J.L. Beck, and S.K. Au. Entropy-based optimal sensor location for structural model updating. *Journal of Vibration and Control*, 6(5):781–800, 2000.

[66] S.T. Quek, S.Y. Wang, and K.K. Ang. Vibration control of composite plates via optimal placement of piezoelectric patches. *Journal of intelligent material systems and structures*, 14(4-5):229–245, 2003.

[67] Anne M. Raich and Tamas R. Liszkai. Multi-objective optimization of sensor and excitation layouts for frequency response function-based structural damage identification. *Computer-Aided Civil and Infrastructure Engineering*, 27(2):95–117, 2012.

[68] A.R.M. Rao and G. Anandakumar. Optimal placement of sensors for structural system identification and health monitoring using a hybrid swarm intelligence technique. *Smart materials and Structures*, 16(6):2658, 2007.

[69] MV Rao, R Samuel, A Ananthan, S Dasgupta, and PS Nair. Nde studies on spacecraft structural components using air coupled ultrasonic and thermography techniques. In *Indian Society for Non-Destructive Testing. Proc National Seminar on Non Destructive Evaluation. Indian: Spyware: Trojans*, pages 1–6, 2006.

[70] Junuthula Narasimha Reddy. *An introduction to the finite element method*, volume 2. McGraw-Hill New York, 1993.

[71] Junuthula Narasimha Reddy. *An introduction to the finite element method*, volume 2. McGraw-Hill New York, 1993.

[72] Gianluigi Rozza, DBP Huynh, and Anthony T Patera. Reduced basis approximation and a posteriori error estimation for affinely parametrized elliptic coercive partial differential equations. *Archives of Computational Methods in Engineering*, 15(3):229–275, 2008.

[73] M Saska, I Ferenczi, M Hess, and K Schilling. Path planning for formations using global optimization with sparse grids. In *Proc. of The 13th IASTED International Conference on Robotics and Applications (RA 2007)*, 2007.

[74] PC Shah and FE Udwadia. A methodology for optimal sensor locations for identification of dynamic systems. *ASME, Transactions, Journal of Applied Mechanics*, 45:188–196, 1978.

[75] GJ Sheu, SM Yang, and WL Huang. Simulating displacement and velocity signals by piezoelectric sensor in vibration control applications. *Smart Materials Research*, 2012, 2012.

[76] S.N. Sivanandam and S.N. Deepa. *Introduction to genetic algorithms*. Springer Publishing Company, Incorporated, 2007.

[77] W.J Staszewski, K. Worden, R. Wardle, and GR Tomlinson. Fail-safe sensor distributions for impact detection in composite materials. *Smart Materials and Structures*, 9(3):298, 2000.

[78] C. Stephan. Sensor placement for modal identification. *Mechanical Systems and Signal Processing*, 2011.

[79] Menner A Tatang. *Direct incorporation of uncertainty in chemical and environmental engineering systems*. PhD thesis, Massachusetts Institute of Technology, 1995.

[80] Anne Teughels and Guido De Roeck. Structural damage identification of the highway bridge z24 by fe model updating. *Journal of Sound and Vibration*, 278(3):589–610, 2004.

[81] S.K. Thyagarajan, M.J. Schulz, P.F. Pai, and J. Chung. Detecting structural damage using frequency response functions. *Journal of Sound and Vibration*, 210(1):162–170, 1998.

[82] Lloyd N Trefethen. Is gauss quadrature better than clenshaw-curtis? *SIAM review*, 50(1):67–87, 2008.

[83] Mengyu Wang and John C Brigham. Assessment of multi-objective optimization for nondestructive evaluation of damage in structural components. *Journal of Intelligent Material Systems and Structures*, page 1045389X13494933, 2013.

[84] Mengyu Wang and John C Brigham. A computational nondestructive evaluation algorithm combining self-evolving parameterization and multi-objective optimization for quantitative damage characterization. *Journal of Nondestructive Evaluation*, pages 1–15, 2014.

[85] Shuang Wang and John C Brigham. A computational framework for the optimal design of morphing processes in locally activated smart material structures. *Smart Materials and Structures*, 21(10):105016, 2012.

[86] Grzegorz W Wasilkowski and Henryk Wozniakowski. Explicit cost bounds of algorithms for multivariate tensor product problems. 1994.

[87] K. Worden and A.P. Burrows. Optimal sensor placement for fault detection. *Engineering Structures*, 23(8):885–901, 2001.

[88] D. Xiu and J. Hesthaven. High-order collocation methods for differential equations with random inputs. *SIAM Journal on Scientific Computing*, 27(3):1118–1139, 2005.

[89] Dongbin Xiu. Fast numerical methods for stochastic computations: A review, 2009.

[90] SM Yang and GS Lee. Vibration control of smart structures by using neural networks. *Journal of dynamic systems, measurement, and control*, 119(1):34–39, 1997.

[91] L. Yao, W.A. Sethares, and D.C. Kammer. Sensor placement for on-orbit modal identification via a genetic algorithm. *AIAA journal*, 31(10):1922–1928, 1993.